

In Situ Characterization of Photomultiplier Tubes for a Dual Phase Xenon Time Projection Chamber in Münster

In situ Charakterisierung der Photomultiplier
einer zwei Phasen Xenon-Zeitprojektionskammer
in Münster

Benjamin Hetz

Bachelor Thesis

Institut für Kernphysik
Mathematisch-Naturwissenschaftliche Fakultät
Westfälische Wilhelms-Universität Münster

November 2013



Referent: Prof. Dr. C. Weinheimer

Korreferent: Prof. Dr. J. Wessels

This is my timey-wimey detector. It goes *DING* when there's stuff.

— The Doctor —

Doctor Who,
Episode 3.10, Blink

Contents

1	Introduction	1
2	Theoretical Background	3
2.1	Evidence for Dark Matter	3
2.1.1	Rotation Curves of Galaxies	3
2.1.2	Gravitational Lensing of the Bullet Cluster	4
2.1.3	Cosmic Microwave Background	7
2.2	Candidates for Dark Matter	8
2.3	Xenon Dual Phase Time Projection Chamber	9
2.3.1	Xenon as Detector Medium	9
2.3.2	Scintillation Process of Xenon	9
2.3.3	Signal Detection	11
2.4	Photomultiplier Tubes	13
2.4.1	Photoelectric Effect	13
2.4.2	Working Principle of a PMT	13
2.5	The XENON Dark Matter Project	15
2.5.1	The XENON100 Experiment	15
2.5.2	The XENON1T Experiment	17
2.5.3	Results of the XENON Experiments	17
3	Experimental Setup	19
3.1	The Xenon Dual Phase Time Projection Chamber in Münster	19
3.2	Signal Measurement	21
3.3	Gain Calibration of the Münster TPC	23
3.4	Data Acquisition	24
4	Analysis	27
4.1	Single Photoelectron Events Candidates	27
4.2	Gain Analysis of a PMT	29
4.3	Gain Equilibration of a PMT	33
4.4	Event Distributions Analysis	34
4.5	Results of the Bottom PMTs	36
4.6	Results of the Top PMTs	36
5	Summary and Outlook	39
A	Photo of the Münster TPC	41

1 Introduction

By today's high precise measurements of the cosmic background radiation by the Wilkinson Microwave Anisotropy Probe satellite (WMAP) and the Planck satellite, it is known that today's universe is composed of 4.9 % visible, baryonic matter, 26.8 % non-baryonic, cold dark matter and 68.3 % dark energy [ESA13]. Whilst the nature of dark energy is still unknown, a lot of theoretical progress has been made to describe the properties of dark matter since its concept was introduced in the 1930's by Fritz Zwicky, due to his observations on the velocity distributions of galaxies inside the Coma Cluster.

Today, one of the most favoured candidates for dark matter, is the weakly interacting, massive particle (WIMP). Though its existing is based upon a solid theoretical basement, its direct experimental detection has not been successful, yet.

This should change by the XENON experiments results. The running XENON100 experiment at the underground laboratory of Gran Sasso (LNGS) has pushed the boundaries for direct spin-independent WIMP-nucleon scattering down to a possible lower cross section of $2.0 \times 10^{-45} \text{ cm}^2$ with a WIMP mass of 55 GeVc^{-2} [XA⁺12a] by using a xenon dual phase time projection chamber (TPC) with an active target mass of 99 kg. The actually assembled successor of the XENON100 experiment, the XENON1T experiment at the LNGS, will go the next step having a target mass of one tonne of xenon. Thus, it will push down the limit on the spin-independent WIMP-nucleon cross section even further to a planned value of $2.0 \times 10^{-47} \text{ cm}^2$ for a WIMP mass of 50 GeVc^{-2} [A⁺10]. The XENON1T experiment will hence become the most sensitive direct WIMP detector being built.

In the group of C. Weinheimer, which is part of the XENON collaboration, at the Institut für Kernphysik from the University of Münster, a dual phase xenon TPC with a target mass of 2.56 kg was built at its xenon lab for research and development purposes concerning purification and calibration techniques, and as a testbed for the XENON1T experiment.

Fourteen photomultiplier tubes (PMTs) have been installed in the detector to detect the primary and the proportional scintillation signals inside the detector. The photomultiplier's gains have been calibrated during the assembly phase of the Münster TPC. But since the gain of a PMT can change with its operation time and environmental parameters, an in situ calibration of the Münster TPC's PMTs would be preferable.

Outline of this Bachelor Thesis

To fulfil the need of an in situ gain calibration method on the PMTs of the Münster TPC, the possibility to use secondary photon events which appear inside the detector for an gain calibration is analysed within this bachelor thesis.

To give background information about the search of WIMPS as dark matter candidates by using a TPC, this thesis starts in chapter two showing the need for the concept of dark matter and why the WIMP is the preferred candidate for it. Also the working principle of a dual phase xenon TPC and its use of PMTs is presented as part of this theoretical background information.

In chapter three the experimental setup used for an in situ gain calibration is described. Starting with an outline of the Münster TPC, an explanation of the data acquisition and data digitization is followed.

The data analysis part of chapter four gives insight of how the event candidates for an in situ gain calibration are selected and how the gain of a PMT and its error can be determined with these event candidates. Furthermore it is described, how the determined gains are used to equalize the gain responses of the PMTs of the Münster TPC.

Chapter five summarizes the new insides of the Münster TPC and the results of its in situ gain calibration.

2 Theoretical Background

This chapter is laying out a theoretical background for this thesis. It is composed of two main parts and starts with justifying the need for dark matter due to today's knowledge of the universe and describes which kinds of dark matter types are known.

In the second half of this chapter the working principle of a dual phase time projection chamber as a direct dark matter detector is explained. And the XENON experiments using this kind of time projection chamber are described.

2.1 Evidence for Dark Matter

Since the 1930's scientists began to realise that the mass distribution of the universe is different than thought before. One of the first evidences of that different mass distribution was given by Fritz Zwicky in 1937 by calculating the masses of the galaxies in the Coma cluster by observing their motion. He found out that his calculations claim that the galaxies have a mass which was four hundred times bigger than his calculations based upon the observation of the visible matter of the galaxies. Due to his calculations he concluded that there must exist some sort of non-visible matter, called *dark matter*, that explains the motion of the cluster's galaxies [Zwi37].

By today's research the universe seems to be composed of 68.3 % of dark energy, 26.8 % of dark matter and only 4.9 % are baryonic matter [ESA13].

2.1.1 Rotation Curves of Galaxies

Besides Zwicky's evidence of the existence of dark matter, Jan Oort's observation on the velocity of stars in the milky way in 1932 [Oor32] was a hint of the existence of dark matter and later in the 1970's Vera Rubin seconds this by showing this behaviour as standard for spiral galaxies [RF70].

By Newtonian mechanics and a given mass distribution $M(r)$ with G being the Newton gravitational constant, one would expect a velocity $v(r)$ for objects of

$$v(r) = \sqrt{\frac{GM(< r)}{r}} \quad \text{with} \quad (2.1)$$

$$M(< r) = \int_0^r M(r') dr' \quad (2.2)$$

for a given distance r from the galactic centre of a galaxy. Because most of the luminous mass of a galaxy is gathered in the galactic centre one would also expect a decrease in the orbital velocity for stars further away from the galactic centre. Nevertheless, a flat

behaviour of the rotation curves for large radii has been observed by spiral galaxies like our milky way. This discrepancy between observations and Newtonian mechanics would be solved by the galaxies having a halo of dark matter surrounding them.

An actual measurement of galaxy NGC 6503 is given in figure 2.1 showing a flat rotation velocity distribution for larger radii r . It is visible that the observed rotation velocity distribution is consistent with a superposition of the galaxy disk and interstellar gas mass distribution by a given radius, if one is also taking the data fitted dark matter halo into account.

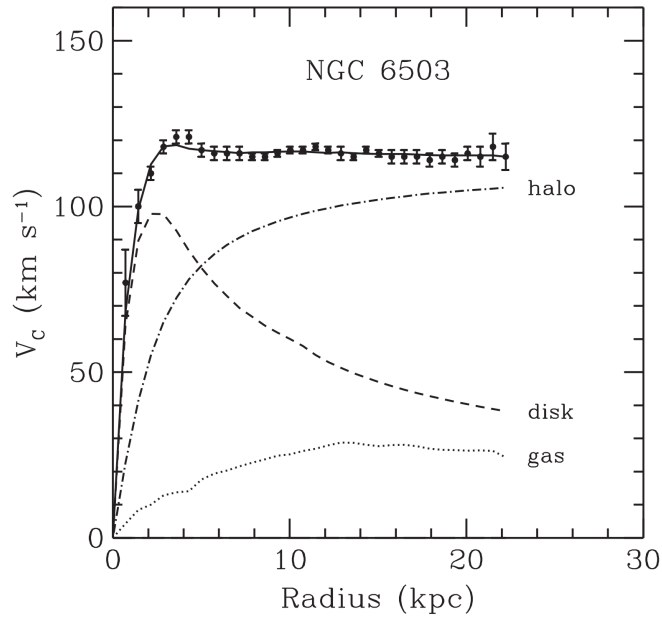


Figure 2.1:

Rotation curve of the spiral galaxy NGC 6503. The points represent the measured data for the rotation velocity in dependence of their distance from the galactic centre. One can see that the rotational velocity stays constant for higher radii which can be described if the superposition of the galaxy disk and interstellar gas mass distribution is enhanced by a dark matter halo [B⁺91].

2.1.2 Gravitational Lensing of the Bullet Cluster

As Albert Einstein published his *Theory of General Relativity*, he predicted that the massless photons' way of propagation through space is affected by gravity [Ein36]. This effect is called *gravitational lensing* and is most likely to be observed if a massive gravitational interacting object is in between the line of sight of a luminous object and the observer of that luminous object.

The gravitational field of the massive objects acts as a gravitational lens and beams of light that are emitted under an angle, in which the beams would normally not be visible by an observer, become visible to him. If the gravitational lensing object is not in the direct line of sight, the observed luminous object may be seen distorted.

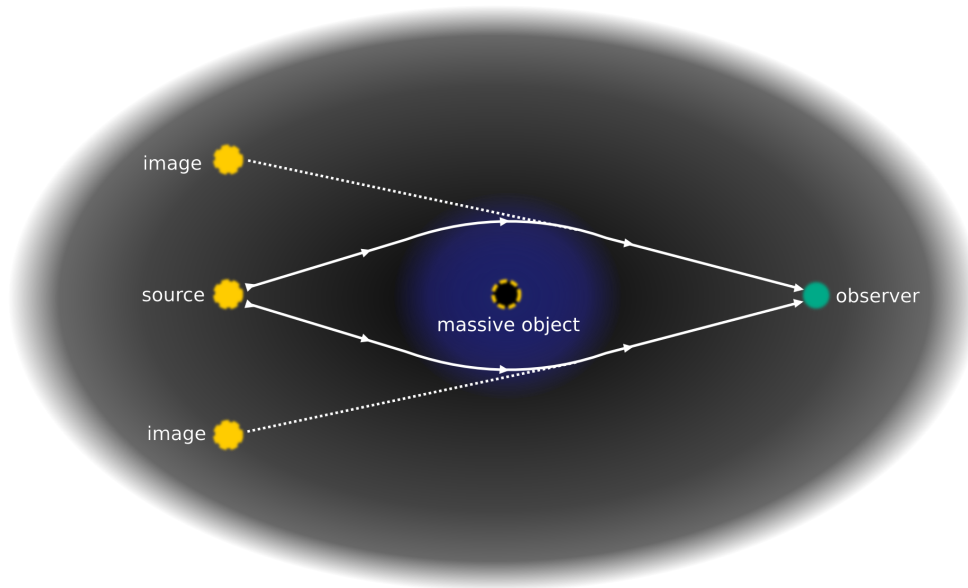


Figure 2.2:

Shown is the basic principle of strong gravitational lensing if a luminous object is hidden behind a strong gravitational interacting object. The luminous object behind the gravitational acting source is seen multiple times under different angles by the observer [Sch11].

That effect is then called *weak lensing*. Another case of gravitational lensing is that the luminous object can be seen as *Einstein rings* by *strong lensing* effects i.e. that the luminous object is seen multiple times arranged in a ring around the gravitational interacting massive object, as it is illustrated in figure 2.2.

The mass causing the gravitational lensing effects can be calculated from measurements of light deflections from the luminous object behind it. If disagreement within this calculated mass and the visible mass measurements –observed for example by x-ray spectroscopy– exists, this can only be explained by the presence of dark matter.

The Bullet Cluster

Evidence of the influence given by dark matter based gravitational lensing, is the observation of collided galaxy clusters being gravitationally bound together. The most famous example for this is the *Bullet Cluster* 1E 0657–558, in which two separate galaxy clusters collided about 150 million years ago. During the collision, the point like stars and planets should have only interacted gravitationally, passing each other non-collisionally.

The dominant mass of galaxy clusters exists in form of hot diffuse gas which is interacting mostly electromagnetically. Thus the gas should slow down its speed of movement and fall back behind during the bypass of stars of each galaxy. Also because of that dominance of the gas masses, the gravitational centres of the passed by galaxies should be concentrated at the corresponding centres of mass.

In figure 2.3 the gravitational potential, measured by weak gravitational lensing, of the Bullet cluster is plotted as green lines and the gas mass distribution is plotted in pseudocolours. Striking are the different locations of the centres of the mass and the gravitation distributions, which is only explainable by the presence of some non-visible, only weakly interacting dark matter which can pass through the collision without slowing down [C⁺06].

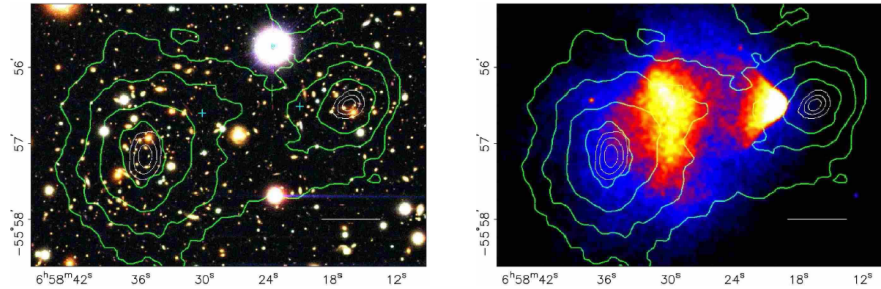


Figure 2.3:

Image of the *Bullet Cluster* 1E 0657—558 showing the remains of the two separate galaxies forming it after their collision. The white bar is a scale indicator of 200 kpc. The gravitational potentials measured by weak lensing are shown in green. The stars and gas clouds are printed in blue respectively in red. Visible is the difference in location of the visible mass distribution and the two centres of gravity [C⁺06].

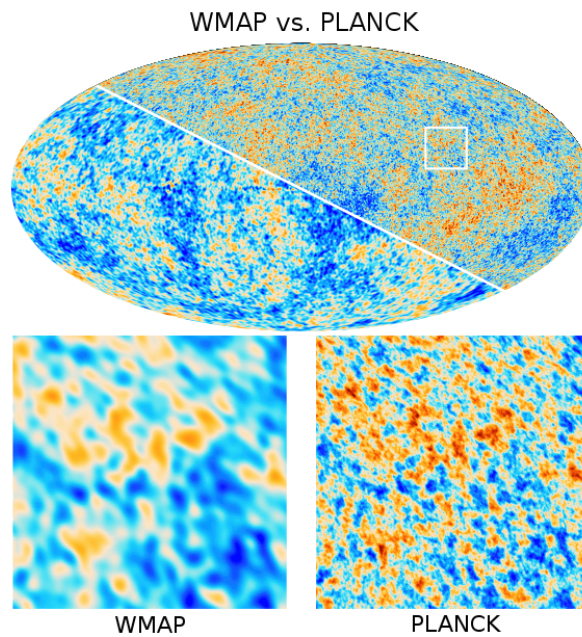


Figure 2.4:

Comparison of the resolution of the CMB measured by WMAP respectively by Planck. Independent of the data's source the next to isotropic distribution of the CMB is visible with fluctuations in a micro Kelvin range which is represented by pseudocolours [ESA13]. Red colours represent hotter areas, while blue colours represent cooler areas.

2.1.3 Cosmic Microwave Background

Penzias and Wilson happened to discover the *cosmic microwave background radiation* (CMB) in 1965 [PW65], that had been predicted by Gamow as thermal radiation leftover from the moment the universe has expanded and cooled down to a temperature, so that the existing photons 380 000 years after the Big Bang have decoupled [Gam48]. These decoupled photons are now seen redshifted and almost isotropically distributed all over the universe. This has been proven with high precision by the *Wilkinson Microwave Anisotropy Probe* (WMAP) satellite and has been second by the even more precise measurements of the *Planck* satellite (see figure 2.4).

Today, the CMB is the best measured black body radiation with a temperature of 2.7255(6) K [PA⁺13]. Its tiny fluctuations on micro Kelvin scale are a relict of the beginning of all later happened cosmical structure building processes of the universe.

Because fluctuations in temperature are in general due to energy density fluctuations, analyses of these temperature fluctuations and the also existing polarization fluctuations of the early universe given by the CMB yields information on the mass distribution of that time. Thus, fitting the angular power spectrum with knowledge of actually cosmological models yield to information about the density distributions of the early universe (for further details on these fitting and analysis methods see [PA⁺13]).

The remarkable result due to this fits of the angular power spectrum is that the total matter component is superseding the baryon density. But because the baryon density is matching the measured luminous density, this is indicating that the non-baryonic matter must also be non-luminous, which indicates the existence of dark matter.

The data acquired by WMAP and Planck so becomes the strongest evidence for a universe containing dark matter and being in strong agreement with the *Lambda Cold Dark Matter Model* (Λ CDM) as standard model of the universe. Planck yields that the quantity of visible matter is superseded by a factor of five from cold (non-relativistic) dark matter (see figure 2.5). Only 4.9% of the universe is ordinary matter, 26.8% is non-baryonic, cold dark matter and the rest of the universe is populated by dark energy, which nature is yet unknown [ESA13].

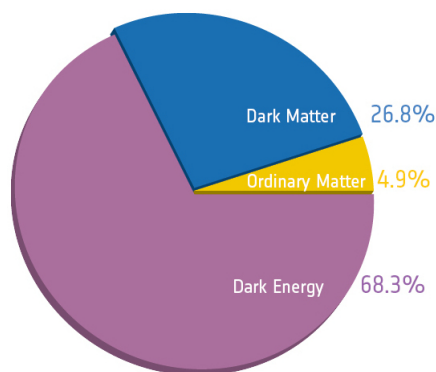


Figure 2.5:

Latest Planck results at time of printing showing the energy and mass distribution of today's universe and the dominance of dark matter over ordinary baryonic matter [ESA13]. The nature of the dark energy is yet unknown.

2.2 Candidates for Dark Matter

The most discussed types of dark matter can be categorised into three classes:

1. *Hot Dark Matter* (HDM) particles are specified by their ultra-relativistic propagation. But most HDM scenarios seem not to be plausible with today's observation of structure formation [WFD83].
2. *Warm Dark Matter* (WDM) propagates at relativistic velocities. Because of this structure building is suppressed until the WDM has cooled down. Thus large structures in the universe have been build first in a so called *top-down-scenario* [DAPR11].
3. *Cold Dark Matter* (CDM) is the dark matter candidate that is describing the observed and simulated *bottom-up-scenario* of structure building during the early universe best, by assuming that it is non-relativistic [OS03] .

All dark matter candidates share the assumption that they do not interact with any kind of electromagnetic radiation. Most of dark matter has to be non-baryonic (see 2.1.3) and does interact gravitationally with ordinary matter thus be able to build today's structures of the universe [OS03]. Also dark matter is assumed to be long-lived and stable on a scale of the age of the universe [OS03].

The WIMP as Dark Matter Candidate

One of the most favoured dark matter candidates is the WIMP (*Weakly Interacting Massive Particle*) [JKG96]. Striking is that the WIMP is a CDM candidate and can therefore describe the structure of today's universe by a bottom-up-scenario [OS03].

The so called *WIMP Miracle* makes them even more favoured by most of today's astrophysicists. During a certain time in the early universe all particles where in thermal equilibration, as was the WIMP. This means the density of WIMPS was high enough, so that its annihilation rate and its production rate were equal. With time the universe cooled and the annihilation-production cycle of the WIMPS slowed down, i. e. it froze out. The time for that freeze out to happen depends on the particles mass.

From this point on, the number of WIMPS decreases dramatically because the existing WIMPS kept annihilating until the density of WIMPS was too small for one WIMP to find another for annihilation and its density stopped dropping. Thus, a certain relic density of WIMPs was left. The physical variable describing the chance of WIMPs finding each other to annihilate is the WIMP's cross section.

The *WIMP Miracle* now is the coincidence that the relic density of a dark matter candidate must have a cross section on the scale of the weak nuclear force. This fits perfectly with the relic density of the only weak interacting WIMPs and their theoretical cross section.

Since the known standard model particles cannot fulfil these needs on a WIMP-like particle satisfactorily, one has likely to look for WIMPs in physics beyond the standard model, like the *supersymmetric theory* (SUSY).

2.3 Xenon Dual Phase Time Projection Chamber

Time projection chambers (TPC) are standard in today's particle physics experiments because this type of detector allows three-dimensional event reconstruction, energy measurement and particle identification [AD09].

Besides existing one phase TPCs the following description will focus on dual phase *liquid xenon* (LXe) and *gaseous xenon* (GXe) time projection chambers, with respect to the working principle of the Münster TPC.

One of the striking advantages of a dual phase TPCs is the possibility to measure proportional light yields by extracting the electrons from primary ionisation processes from the LXe phase into the GXe phase and thus yielding more information on the particles properties.

2.3.1 Xenon as Detector Medium

Advantages of LXe as detector material over other mediums, like semiconductors etc, is its high atomic number ($Z = 54$) and its high density (approximately 3 g cm^{-3}) given over a homogeneous volume, thus having a natural self-shielding against external radiation [AD09] and therefore allowing fiducial cuts based on the LXe volume used for a given TPC.

Also the sensitivity of a xenon TPC can be scaled by its volume, with the price of pure xenon and the increasing space needed being the most limiting factors.

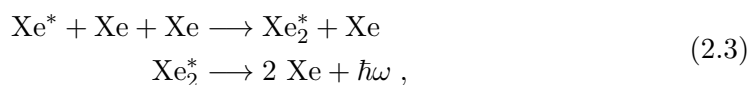
The existence of nearly 50 % odd and 50 % even xenon isotopes allows a xenon TPC to do measures on spin dependent and independent particle interactions likewise.

Furthermore, the emission bands of LXe and GXe are almost identical, with a peak maximum at a wavelength of approximately 178 nm (see figure 2.6), so that similar detection mechanism can be used for both phases.

2.3.2 Scintillation Process of Xenon

The process of an energetic particle exciting an atom which then emits a photon during its relaxation is called scintillation.

Like all noble gases xenon does not scintillate by relaxing from one excited xenon atom state, but by relaxing from an excited dimer state, called excimer. This relaxation in the LXe phase can be described by following formula:



with the (*) marking the excited states and $\hbar\omega$ being the scintillated photon with a wavelength of 178 nm [AD09].

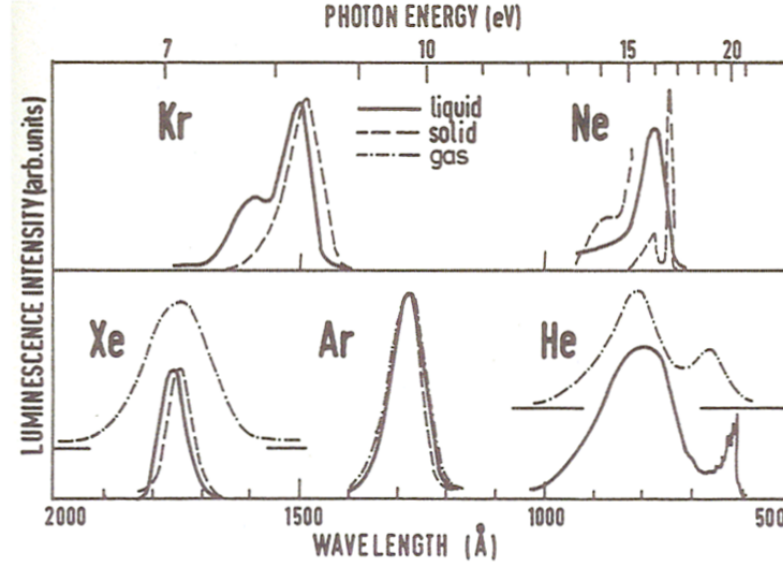
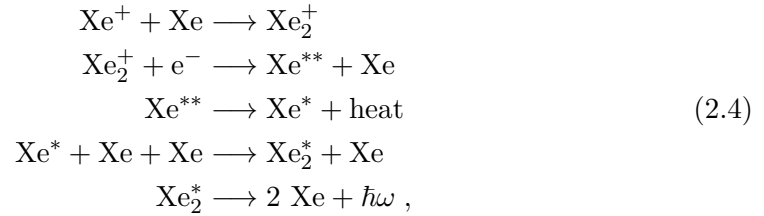


Figure 2.6:

Emission bands of the liquid, gaseous and solid phase of noble gases. Striking is the nearly identical emission wavelength of xenon in all three phases compared to the other noble gases. Only argon's emission bands can compete with that, but it has other deficits compared to xenon, like a lower atomic number and density in the liquid phase thus being less self-shielding against radiation penetration [AD09].

By high enough energies, so that a xenon atom gets ionized, a scintillation photon of the same wavelength can be observed and be described by the process [AD09]:



with $(^+)$ marking the ionized state of a xenon atom and e^- being a free electron.

Signals of the scintillation process taking place in the LXe phase are referred to as *S1 signals*.

The scintillation in the GXe phase, the so called *proportional scintillation*, is stimulated by an electron cloud which has been produced by ionizing processes in the LXe phase. These electrons drift with a constant velocity in the detector to the GXe phase because of an applied electric field induced by a gate grid placed outside the LXe phase and inside the GXe phase. Reaching the phase interface of LXe and GXe the electron cloud is furthermore extracted from the LXe phase into the GXe phase by an anode grid. Due to this extraction the signal is effectively amplified and its extraction efficiency is 100% for electric field strengths of more than 10 kV cm^{-1} [AD09]. This proportional signal is usually referred to as *S2 signal*.

The number of proportional scintillation photons N_γ is proportional to the energy deposition of the particle triggering the ionization inside the LXe phase and is given by [AD09] as

$$N_\gamma = \alpha N_e \left(\frac{\varepsilon_e}{p} - \beta \right) px, \quad (2.5)$$

with N_e being the number of electrons extracted into the GXe phase, α and β being material factors, ε being the electric field inside the TPC, p being the pressure and x being the drift length of the electrons inside the GXe phase.

2.3.3 Signal Detection

The signal detection of the S1 and S2 signals is done by two separate arrays of *vacuum ultra violet* (VUV) sensible PMTs, i. e. the PMTs most sensitive detection wavelength range is that of the xenon scintillation light, which are placed at the top and at the bottom of the detector.

At this point another beneficial property of LXe should be mentioned, which is its high refractive index of about 1.62 [S⁺04]. Because of this a lot of internal reflection is taking place on the surface of the LXe phase and next to all scintillation light from the LXe phase is detectable uniformly distributed over all bottom PMTs. Thus the total light yield detected by the bottom PMTs gives information about the total energy deposition inside the detector. This information can then for example be used to do spectroscopy within the detector.

Most of the signals seen by the top PMTs are S2 signals which are very localized detected by single PMTs of the top PMT array, thus providing information about the signals event localization in the x-y plane with a resolution of centimetres to millimetres depending on the form of the PMT array and the size and resolution of the single PMTs [AD09].

The depth information (z-axis) of the primary scintillation event is reconstructed from the difference in time of the primary S1 signal and the secondary S2 signal. This is possible because of a next to constant electron drift time by a given constant field strength. The reconstructed depth of the particle event can have a resolution better than one millimetre [AD09].

Furthermore discriminations of the type of incoming particles into the detector is possible by looking at the ratio of the amplitude of the S1 and the S2 signal. A schematic of this showing the difference of a WIMP/Neutron recoil like and electron recoil like S1 and S2 signal is presented in figure 2.7.

An illustration of all these processes taking place inside a dual phase xenon TPC is presented in figure 2.8. The S1 and S2 signals are shown, as is an example electron cloud drifting to the extraction anode. Furthermore both PMT arrays are shown, which are registering the S1 and S2 waveforms sketched on the timeline to the left of the figure.

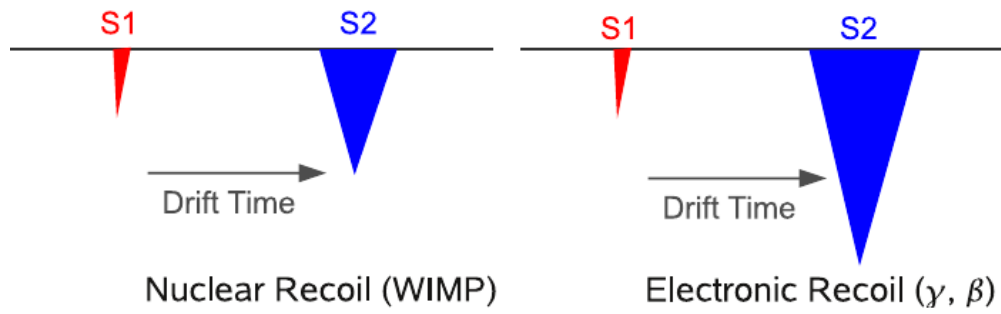


Figure 2.7:

Illustration of the different S1 to S2 signal ratio of WIMP/Neutron recoil like and electron recoil like events inside a xenon TPC [XA⁺12b].

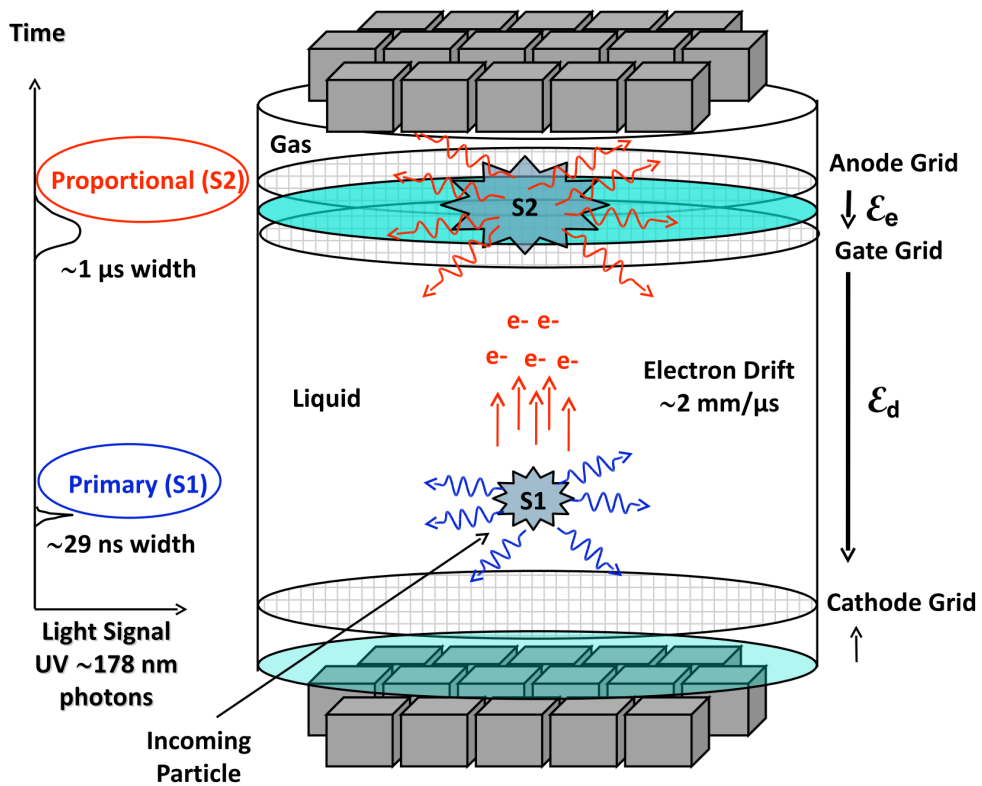


Figure 2.8:

Schematic of the working principle of a xenon dual phase TPC. A particle causes primary S1 signal scintillation and liberates electrons due to ionization inside the LXe phase. These electrons drift due to the electric field gate and cathode grid to the LXe surface. Reaching it, they are extracted by the anode grid field and yield proportional scintillation S2 signal light. Both signals are registered by the two PMT arrays at the top and the bottom of the detector. Furthermore a schematic of the signal width, amplitude and appearance in time is shown [A⁺11].

2.4 Photomultiplier Tubes

Photomultiplier tubes are the detectors for the scintillation light of the Münster and the XENON TPCs. Thus it is important to understand the working principle of a PMT, which is described in the following section.

2.4.1 Photoelectric Effect

A photon can interact with an electron bound to a nucleus by exciting the bound electron to a higher energy level of that atom. If the energy of the photon is more than the work function needed for that electron, the electron escapes from the atom. The kinetic energy E_{kin} of that free electron is given by the difference of the energy $\hbar\omega$ of the photon and the work function W as

$$E_{\text{kin}} = \hbar\omega - W . \quad (2.6)$$

The work function W is defined by [Kit10] as difference between the vacuum energy E_{vac} and the fermi energy E_{fermi} as

$$W = E_{\text{vac}} - E_{\text{fermi}} . \quad (2.7)$$

The cross section σ_{photo} for the photoelectric effect is related to the proton number Z of the electron's nucleus and the photon energy $\hbar\omega$ by

$$\sigma_{\text{photo}} \propto \frac{Z^5}{(\hbar\omega)^{7/2}} . \quad (2.8)$$

2.4.2 Working Principle of a PMT

The registration of light signals by a PMT is done using the photoelectric effect. Also a PMT is capable to register single photons and convert them into an electric signal.

A schematic of a PMT is shown in figure 2.9. The front of a PMT is usually screened by a transparent shield. Behind that shield a photo cathode is following, in which the photon is interacting with its material, emitting an electron out of it by photoelectric effect. The emitted electron is afterwards focused by focusing electrodes and accelerated to an array of dynodes which are connected by a chain of resistors giving each dynode the same more positive potential than the last one. Because of the raising potential of the dynodes the initial electron is first hitting the first dynode thus more *secondary electrons* are emitted from this dynode and these electrons are now accelerated to the next dynode repeating that step of electron multiplication until they reach the anode with the maximal potential. On the anode one can measure a voltage that is proportional to the initial number of photoelectrons.

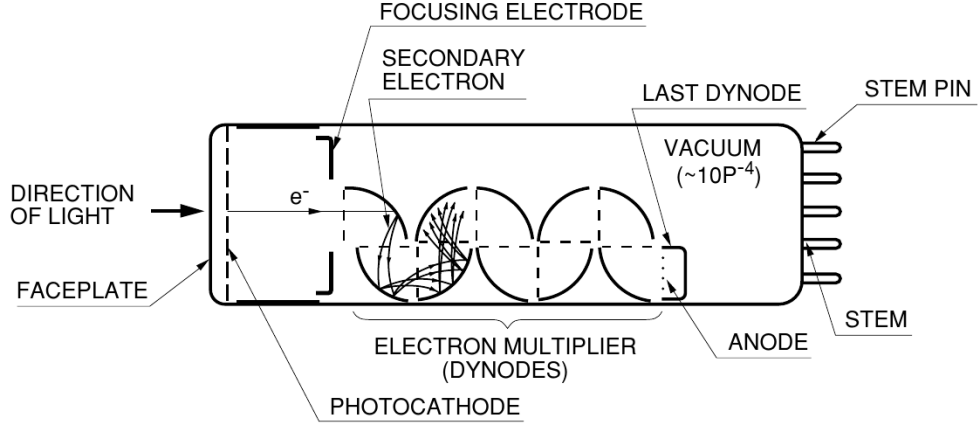


Figure 2.9:

Schematic of a PMT working principle. Shown is the photoelectron created by the photoelectric effect of the incident photon. Furthermore the avalanche like effect that liberates more electrons every dynode stage is shown [Ham07].

Using an actually build PMT, not every photon of sufficient energy does trigger the photoelectric effect. The probability to trigger such an event is called quantum efficiency η and is the ration

$$\eta(\nu) = \frac{N_{pe}}{N_{ph}} , \quad (2.9)$$

with N_{pe} being the number of created secondary photoelectrons emitted from the photocathode and N_{ph} being the number of photons that enter the PMT detection area. The quantum efficiency depends also on the frequency ν of the entering photons and the used materials of the PMT.

Moreover the collection efficiency ϵ of a PMT is to mention. It is defined as

$$\epsilon = \frac{N_{dy}}{N_{pe}} , \quad (2.10)$$

with N_{dyn} being the number of secondary electrons due to the photoelectric effect at the first dynode of a PMT and N_{pe} being the initial number of photoelectrons from the cathode. An important characteristic of a PMT that needs to be known, is its gain g , i. e. the ratio of charge on the anode compared to the number of incident photoelectrons. This is described by the formula

$$N_e = g \cdot N_{pe} , \quad (2.11)$$

with N_e being the number of electrons collected by the anode. A way to determine a PMT's gain g is hence to create *single photon events* (SPE) on the first PMT dynode.

A common way to determine the gain of a PMT is to place it in a dark box with a LED inside. This LED is then illuminating the PMT by very short (a few nanoseconds) light pulses. The PMT's data acquisition is hereby triggered by the toggle event of the

LED's supply voltage. For a successful gain calibration the light intensity is lowered to a level in which the PMT is not registering any photons in 90 % to 95 % of the time. The other 5 % to 10 % of the emitted photons lead to a single photoelectron response inside the PMT and next to no photons are registered as multiple photoelectrons responses by the PMT in the dark box.

With this technique Johannes Schulz calibrated all 14 PMT's gains of the Münster TPC in the year 2011 at room temperature in his diploma thesis [Sch11].

Besides the material characteristics of the PMT, also the applied high voltage to the PMT's dynodes is shaping the gain amplification obeying a power law of the form

$$g = A \cdot U^k, \quad (2.12)$$

with A being an amplification factor, U being the applied voltage and k being a parameter determined by the material, structure and number of the dynodes.

2.5 The XENON Dark Matter Project

The XENON Dark Matter Collaboration comprised of sixteen international partners is operating one of today's most sensitive WIMP direct detection experiments, the XENON100 detector in an underground laboratory at the *Gran Sasso National Laboratory* (LNGS) in Italy.

Its predecessor, the XENON10, was the first experiment using a dual phase TPC for direct detection of WIMPS as dark matter candidates and was also located at the LNGS. The successor of XENON100, the XENON1T experiment, is under construction at the LNGS, too.

2.5.1 The XENON100 Experiment

The XENON100 experiment is a cylindrical dual phase xenon TPC with a diameter and height of 30 cm each and a total target mass of 62 kg LXe. The inner target mass is surrounded by an active 99 kg xenon veto scintillator with 64 PMTs monitoring this veto volume [XA⁺12b].

Besides the 3700 m water equivalent, given by the location in the underground laboratory of Gran Sasso mountain, which reduces the muon flux by a factor of 10^6 [XA⁺12b], fiducial cuts on the target volume are done to reduce the background further [XA⁺12b]. An example of a possible fiducial cut and an event distribution reconstruction inside the XENON100 detector of a 225 day run is shown in figure 2.10.

For maximum light collection efficiency the separation that surrounds the target from the veto volume is made of *polytetrafluorethylen* (PTFE) which has very good VUV reflection properties and which is also a good electrical insulator [XA⁺12b].

The signal detection is done by two arrays of Hamamatsu R8520-06-A1 1" square PMTs, which have been selected because of their low intrinsic radioactivity [XA⁺12b]. The 98 PMTs on the top array are located inside the GXe phase in concentric circles, giving a good photocathode coverage of the radial surface of about 44 %. This allows a good event location reconstruction because of the localized detected S2 signals [XA⁺12b].

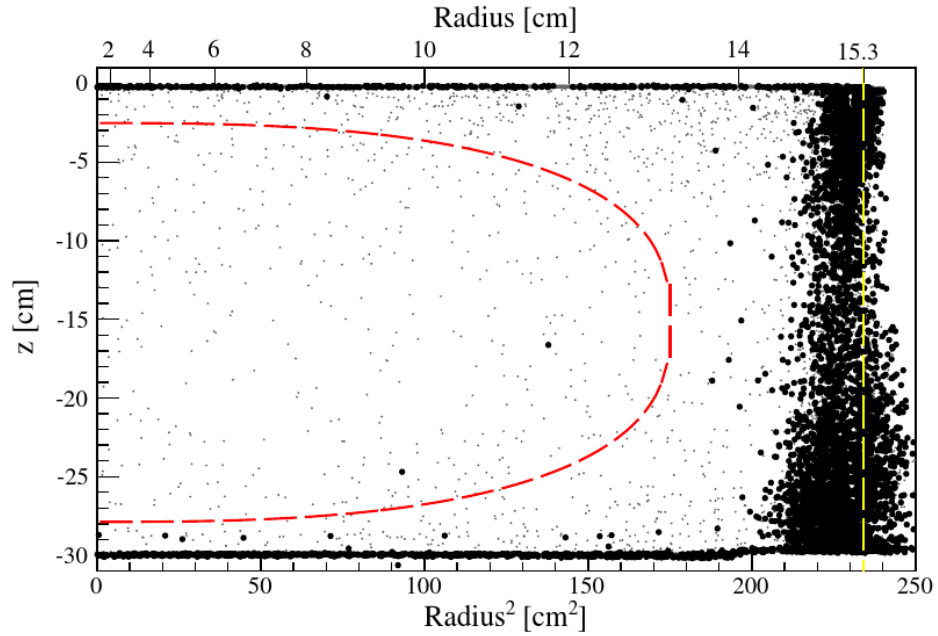


Figure 2.10:

Distribution of all events (dots) that had been registered by the XENON100 detector during a 225 day run in the years 2011 and 2012. A 34 kg target mass fiducial cut is represented by the drawn red dashed line inside the detector volume. The two bold dots inside this fiducial volume are possible WIMP candidates that pass all quality criteria for single-scatter nuclear recoils. Nevertheless, they fall into the expected background rate [XA⁺12a].

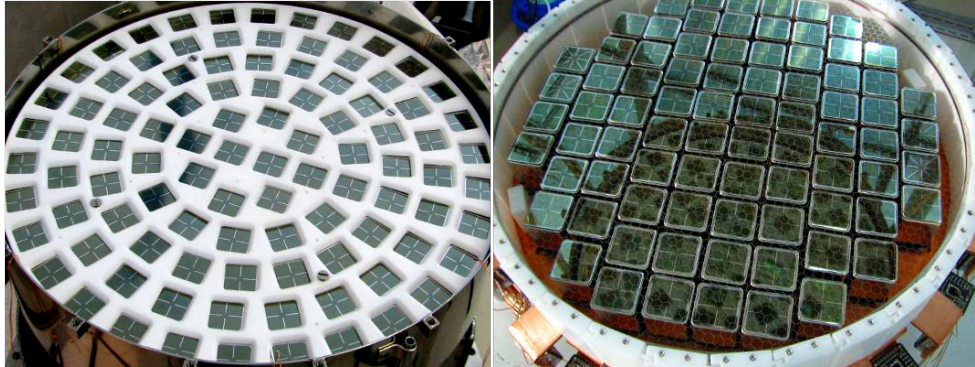


Figure 2.11:

Left: Photo of the arrangement of the top PMT array in concentric circles for optimal position reconstruction.

Right: Photo of the arrangement of the bottom PMT array in a grid for a maximum area coverage to provide best light collection [XA⁺12b].

The bottom array is equipped with 80 PMTs arranged in a grid inside the LXe phase under the detectors cathode, which provides an average PMT photocathode coverage of 52% and thus giving an efficient S1 light collection [XA⁺12b].

A picture of both PMT arrays showing their arrangement is given in figure 2.11.

2.5.2 The XENON1T Experiment

The next generation of the XENON experiments is the XENON1T detector that is actually under construction and will be located at the LGNS, too.

As mentioned in section 2.3 a possible step to increase the sensitive of a xenon TPC is to raise the amount of xenon it uses as target mass and this step is consequently taken by raising the total amount of xenon to a mass of 2.4 tonnes in the XENON1T experiment. This new detector will have a diameter of one meter and a height of one meter. It will only use one of its 2.4 tonnes of xenon as fiducial mass [A⁺10] and another 400 kg of its xenon mass will be used as active veto, similar in concept to the XENON100 experiment. [A⁺10].

An additional water tank with about 5 m of water in all directions around the detector will stop gamma and neutron radiation from the rocks of Gran Sasso Mountain [A⁺10]. Furthermore another veto source is given by the water tank, because it serves as active muon-veto by detecting the Cherenkov light radiation from cosmic muons travelling through the water tank and hence possibly through the detector itself, too [A⁺10].

Moreover, the total amount of PMTs will be increased to 242. Half of the PMTs will be located in the bottom array inside the LXe phase and half of them in the top GXe phase [A⁺10]. The arrangements of this two PMT arrays is plant to be similar to the XENON100 PMT arrays with optimal positioning reconstruction and light collection probabilities in mind.

2.5.3 Results of the XENON Experiments

The goal of the XENON100 experiment to become the worlds most sensitive direct detector of WIMPs as dark matter candidates has been reached, by setting the upper limit for a spin-independent WIMP-Nucleon scattering cross section to a value of $2.0 \times 10^{-45} \text{ cm}^2$ for WIMPS with a mass of $55 \text{ GeV}/c^2$ [XA⁺12a] and thus reaching its designed level of sensitivity [XA⁺12b].

Though no definitive WIMP detection has happened so far, most results of other experiments that claimed to have seen signs of WIMP interactions, became implausible due to the XENON100 results (see figure 2.12).

Independent confirmation of the XENON100 results have just been published recently in October 2013 by the *Large Underground Xenon dark matter experiment* (LUX) [L⁺13]. The LUX experiment also uses a dual phase xenon TPC but with a xenon volume of 370 kg and it has set a new 90% confidence limit on the spin-independent upper limit on the cross section of $7.6 \times 10^{-46} \text{ cm}^2$ at a WIMP mass of $33 \text{ GeV}/c^2$ [L⁺13].

The sensitivity goal of the, currently under construction, XENON1T experiment is to set an upper limit on the spin-independent WIMP-Nucleon scattering cross section of $2.0 \times 10^{-47} \text{ cm}^2$ [A⁺10]. Being built, the XENON1T will thus supersede the LUX experiment and become the most sensitive direct detector of WIMPs.

Also the sensitivity in the low mass WIMP region will increase dramatically for the XENON1T experiment compared to the XENON100 experiment, as seen in figure 2.12. The figure also shows the actual sensitivity boundaries of the former XENON10 and other experiments limits on the WIMP cross section. The actual XENON100 upper limit on the WIMP-Nucleon cross section is printed as blue line and the expected one of the XENON1T experiment as a dashed red line. Preferred parameter spaces are marked in grey and it becomes clear that the XENON1T experiment will cover large parts of them.

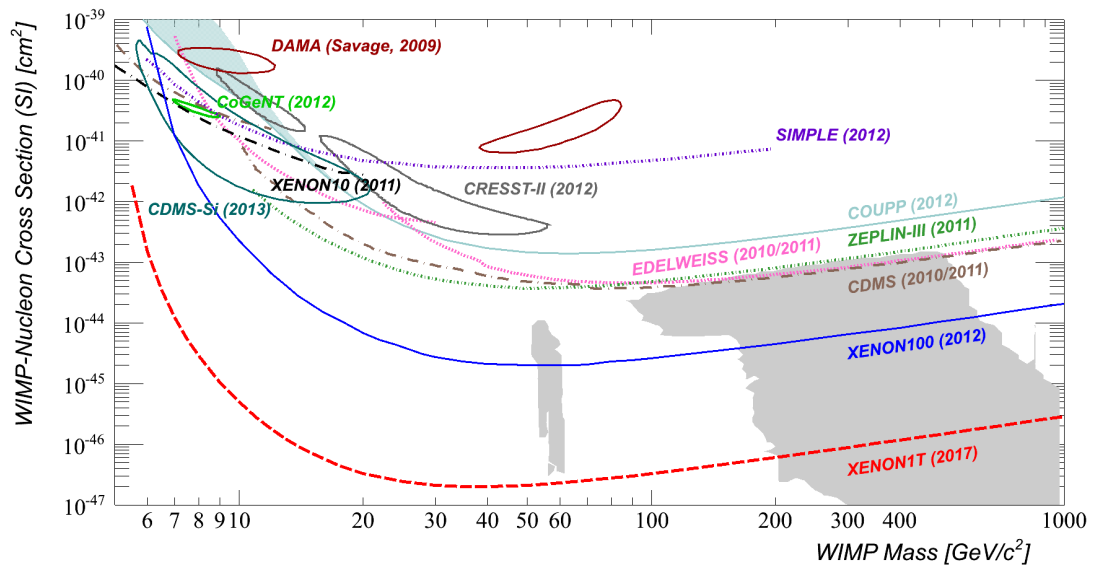


Figure 2.12:

Sensitivity plot of different experiments looking for dark matter. Shown is the exclusion graph of the XENON100 experiment and the new planned sensitivity of the XENON1T experiment that is actually under construction. The gray areas are the most preferred parameter spaces for WIMP candidates and it is visible that the XENON1T experiment will cover large parts of them [A⁺10].

3 Experimental Setup

3.1 The Xenon Dual Phase Time Projection Chamber in Münster

In the year 2011 the building of a Dual Phase Time Projection Chamber in the *Institut für Kernphysik of the University of Münster* has started in the context of Johannes Schulz' diploma thesis [Sch11]. A photo of the Münster TPC today in the Münster XENON laboratory can be found in the appendix figure A.1.

Its design frame was adapted from the TPC detectors of the XENON Project, but reconfirmed and resized to the specific setup in Münster with the goal in mind to be a testbed for the XENON1T experiment. Thus all used parts were selected to meet the same low radioactive requirements as the XENON1T parts [Sch11].

The built Münster TPC has an empty weight of 2.56 kg, a height of 170 mm and a diameter of 80 mm. The TPC's inner is build up from a stack of 23 white PTFE (Teflon) slices, which were especially chosen because of PTFE's high VUV reflection properties and its good electrical insulator properties [XA⁺12b]. A figure of the inner of the TPC respectively of its PTFE slices is given in figure 3.1.

To create the drift and extraction field inside the detector, four meshes of 2.62 mm pitch, 150 μm thickness and 150 μm wire diameter were welded by eight spots onto steel rings with ConFlat CF100 size, which means they have an inner diameter of 101.8 mm, an outer diameter of 120.5 mm and a thickness of 2 mm.

The field creating parameter for the bottom cathode mesh is given by a negative potential of -10 kV . The central gate mesh is at ground potential and the anode one, for extracting the electrons from the LXe phase into the GXe phase, is at a potential of 4 kV at a height of 5 mm above the gate mesh. A fourth screening mesh is placed 5 mm above the anode mesh.

Due to the 8 kV cm^{-1} strong electric field between the anode and the gate mesh, an electron extraction rate for proportional scintillation of about 90% from the LXe into the GXe phase is achieved [AD09].

The electric field of 0.8 kV cm^{-1} inside the detector itself, which is given by the bottom cathode mesh and the top gate mesh, gives a constant electron drift velocity of approximately $2\text{ }\mu\text{m s}^{-1}$ [AD09]. That means that the maximum possible electron drift time inside the Münster TPC's LXe phase is 85 ms.

Embedded inside the PTFE stack are 12 oxygen free, high conductivity cooper rings. Connected by $1\text{ G}\Omega$ resistors, the cooper rings work as a voltage divider thus shaping the detector's inner electric field. Striking at that point is that to fulfil the low radioactivity requirements, the resistors are not soldered but crimped or plugged [Sch11].

The whole TPC is connected to a cooling tower which is a Gifford-McMahon type cold head with a self-produced cold finger made of cooper. The TPC and the cooling tower itself are placed into a steel vessel with a diameter of 270 mm and a length of 1500 mm with an insulation vacuum produced by a turbomolecular pump and a rotary vane pump [Sch11].

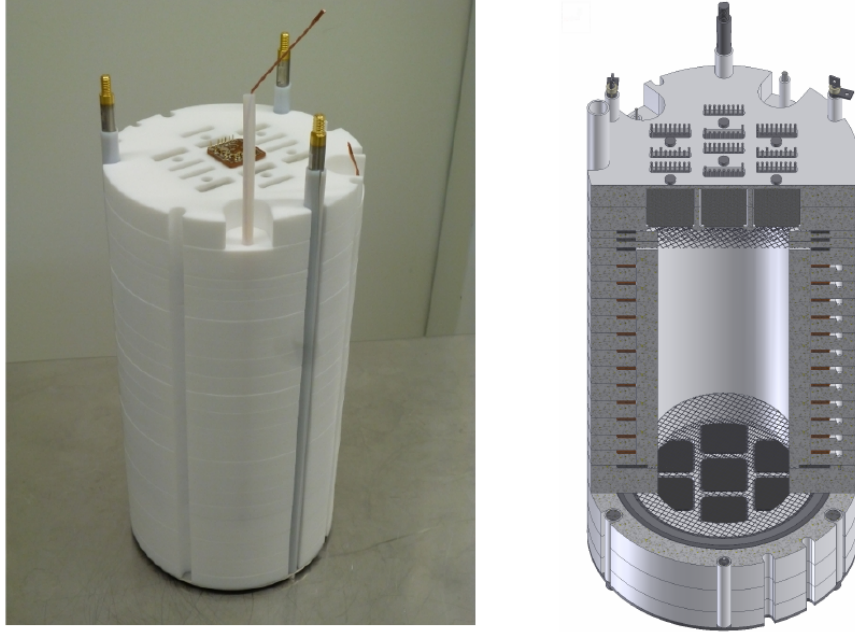


Figure 3.1:

Figure of the PTFE stack and the arrangement of the PMTs inside the Münster TPC. On the left a picture of the assembled PTFE stack is shown and the connections of the PMTs of the upper array are visible. On the right a schematic of the PTFE stack and its inner is shown. One can see the electric field shaping cooper rings embedded between the single PTFE slices. Furthermore, the ring like arrangement of the PMTs is visible for the bottom array and the meshes are shown, too [Sch11].

PMTs of the Münster TPC

For the detection of the primary S1 and the proportional S2 scintillation light inside the detector two arrays of 14 PMTs are used in total.

The used type of PMTs are one inch squared, Hamamatsu R8520-06-AL PMTs, with ten dynode stages. This means the used PMTs at the Münster TPC are identical to the PMTs that were initially selected for the XENON100 experiment because of their low intrinsic self-radioactivity [XA⁺12b]. A further technical feature of the used PMTs is their possible operation temperature range from $-110\text{ }^{\circ}\text{C}$ to $50\text{ }^{\circ}\text{C}$, thus being compatible with a xenon TPC's cryogenic temperature [XA⁺12b]. The bialkali photo cathode has an effective area of $(20.5 \times 20.5)\text{ mm}^2$ which is covered with a front screen made of silica glass so that it is transparent to VUV photons.

Furthermore, the photocathode has been specially designed to be most sensitive in the wavelength range of 160 nm to 650 nm with a quantum efficiency of approximately 30 % and a collection coefficient of 70 % for 178 nm wavelengths. This is most convenient since it is the wavelength emitted by the xenon scintillation processes.

The PMTs are placed in the form of two arrays inside the detector. One array of seven PMTs at the top of the detector inside the GXe phase and another similar array of seven PMTs is placed at the detector's bottom inside the LXe phase. Each array is forming a ring like structure of six PMTs with another, the seventh, PMT in its centre. This formation gives an photocathode coverage for the top and the bottom of 56 %, which gives the possibility for good three dimensional event reconstruction and light collection [Sch11].

A schematic of this two PMT arrays inside the Münster TPC is shown in figure 3.1.

3.2 Signal Measurement

The digitization of the PMT's signal response is done by two CAENV1724 14 bit, 100MHz, 8 Channel digitizer and 2.25 V full scale boards build by CAEN Electronic Instrumentation¹.

Although the boards are capable of transmitting the data zero length encoded by hardware functionality, that feature was not used to conserve the original recorded waveform with its whole signal bandwidth.

Following steps are run, if a signal, big enough to trigger the digitizers, is detected on one PMT channel: First, both digitizer boards start digitizing the signal of all 14 PMTs. This is realized by cross connecting the external trigger ports of both digitizer boards.

The digitized waveform of the photoelectron induced current I is made out of 512 sample points, with 112 points being sampled before and 400 points being sampled after the trigger signal. With a given sample rate of 100 MHz the total recorded waveform length then equals 5.12 μ s in the time domain. Integrating the voltage drop U over a given resistance R of the PMT's connection over the sample time interval Δt of the waveform yields to the total charge output

$$Q = \int_{t_1}^{t_2} I dt = \int_{t_1}^{t_2} \frac{U}{R} dt \quad (3.1)$$

for a single PMT waveform. Equal for a discrete sampled waveform with f sample points and a sample interval time Δt is

$$Q = \sum_{i=0}^f \frac{U_i \cdot \Delta t}{R} . \quad (3.2)$$

¹CAEN-Tools for discover; URL: <http://www.caen.it/>

For the used experimental setup this leads to

$$Q = \sum_{i=0}^{512} \frac{2.25 \text{ V} \cdot 10 \text{ ns}}{2^{14} \cdot 50 \Omega} \cdot N_{\text{ADC}} \quad (3.3)$$

$$= 2.75 \times 10^{-14} \text{ C} \cdot N_{\text{ADC}} , \quad (3.4)$$

with N_{ADC} being the measured ADC counts representing the voltage drop U over the full range of 2.25 V by a digitizer resolution of 14 bit. That gives a voltage resolution of 0.14 mV per ADC count. The calculated total charge output can be expressed in numbers of elementary charges N_e by

$$N_e = \frac{Q}{e} = 171428 \cdot N_{\text{ADC}} . \quad (3.5)$$

These calculations of the raw digitizer data are done automatically by a *raw data processor* which had been programmed by Dr. Ethan Brown of the University of Münster especially for the Münster TPC using the ROOT² analysis toolkit of the CERN³ organisation.

To have a common baseline for all 14 digitised PMTs' signals, the mean of the 112 sample points, that have been recorded before the detected signal, is calculated for each single PMT individually by the raw data processor and is then subtracted from the raw waveform. In Figure 3.2 a complete processed waveform is given as an example of the processing done by the raw data processor.

On top of that elementary processing work the raw data processor also includes a peak identification algorithm sorting the events into S1 and S2 like signals. The used peak finding algorithm is identical in function to the one used in the XENON100 experiment described in [XA⁺12b]. It starts with summing up all processed waveforms of each PMT. Afterwards a digital low-pass filter is applied to help the peak finding algorithm looking for signals that exceed a threshold of 10 mV for more than 600 ns [XA⁺12b].

For the validation of the found signals as possible S2 peak candidates, the peaks average amplitudes have to be lower than 25 % of its maximum peak value for 210 ns before and after its mean value [XA⁺12b]. For all peak candidates with a *full width at half maximum* (FWHM) of more than 350 ns, parameters like the position of the waveform, area and width, etc. are calculated and saved into a ROOT defined, binary data file format. By this FWHM restriction possible afterpulses, multiple scatterings and single electron events are removed from the data set [XA⁺12b].

The S1 candidate peak finding is done afterwards by analysing all yet again unfiltered waveforms. Because S2 signals greater than about 3 V (≈ 300 PE) and their afterpulses can make the S1 pulse identification of the raw data processor difficult, only the time interval before that large S2 peak is analysed [XA⁺12b]. For the identification of a signal as S1 candidate the summed waveforms are scanned for peaks exceeding a threshold of 3 mV (≈ 0.3 PE) and the area around that possible S1 candidate is analysed to reject

²ROOT-A Data Analysis Toolkit; URL: root.cern.ch

³CERN-Accelerating science; URL: cern.ch

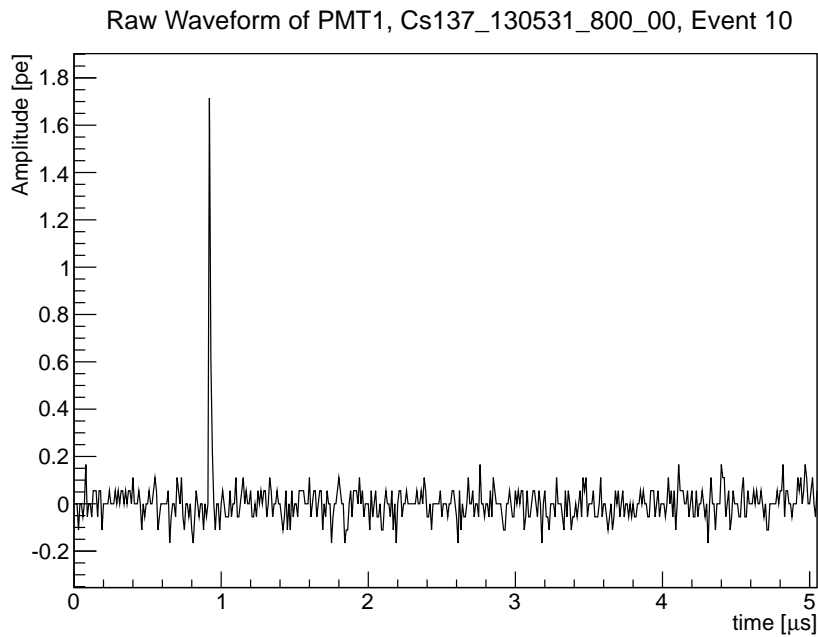


Figure 3.2:

Example of a complete raw waveform of PMT 1 of the Münster TPC showing a S1 Signal. The digitizers raw data has already been run through the raw data processor at this stage.

false signals from background fluctuations by electronic noise [XA⁺12b]. Afterwards parameters like the waveform position, area and width are calculated and saved into the same ROOT file as it has been done with the S2 peaks information.

3.3 Gain Calibration of the Münster TPC

The gain response is likely to change by the PMT's environmental temperature –due to not negligible resistance and capacity changes at cryogenic temperatures– and also due to the fact that the gain of a PMT changes with its operation time as shown in [Mas08]. Accordingly, an in situ calibration technique for the Münster TPC's PMTs is preferable.

Because the Münster TPC has no optical fibres build into the detector's inner, which are connected to outer LEDs creating short light pulses of a suitable wavelength of about 470 nm, like the XENON100 experiment has [XA⁺12b], another way to create single photoelectron events (SPE) inside the Münster TPC must be found.

One candidate for an in situ gain calibration possibility was found by looking at standard calibration measurements at the Münster TPC previous to this bachelor thesis [Bro13].

It has been observed that besides the main primary S1 signal produced by interactions induced by a calibrations source placed outside the detector, one can see secondary S1 signals that are small in amplitude inside some of the acquired waveforms. An example of a waveform containing this secondary S1 signals showing up after a primary S1 signal is given in figure 4.1. Judging by the amplitude of these secondary S1 signals and some preliminary energy distribution plots done, with that secondary S1 pulses, the idea came up to investigate these S1 signals in more detail.

Though not knowing the primary reasons where these secondary S1 pulses are originated from, it seemed promising that they could be SPE detected by the Münster TPC and though giving a possible starting point to find a way for an in situ calibration of the Münster TPC's PMTs [Bro13].

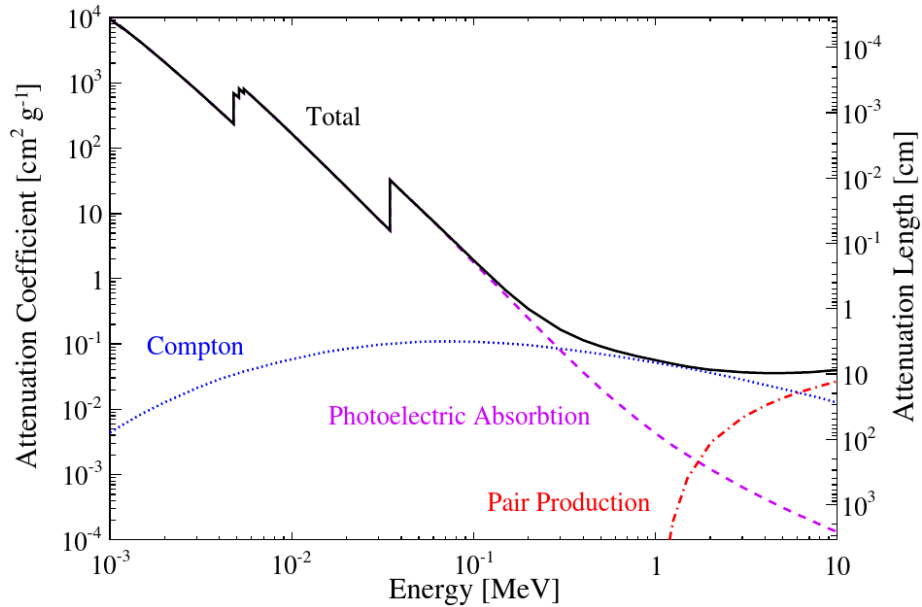


Figure 3.3:

Plot of the attenuation coefficient of Xenon. The black line is showing the total γ -ray mass attenuation coefficient xenon as a function of energy. The dashed violet line is representing the photoelectric absorption, Compton scattering is given by the dotted blue line and pair production by the dashed-dotted red one. The right scale is showing the attenuation length in liquid xenon [Pla12].

3.4 Data Acquisition

For further investigations of these possible SPE in this thesis a *Caesium-137* (Cs137) calibration source with an activity of 441 kBq, emitting 662 keV γ -rays, was used to produce signals inside the detector. The Cs137 source was therefore placed outside of the vacuum cryostat which surrounds the TPC, so that it was located at about the half height of the detector.

The Cs137 source has the advantage that its emitted 662 keV γ -rays have an attenuation length of approximately 10 cm in LXe (see figure 3.3). In the special case of Münster's TPC the Cs137 source emitted γ -rays have to pass through the steel walls of the cooling tower setup and thus the highest energy deposit of emitted γ -rays should take place inside the detector because of its diameter of 8 cm.

To make sure that no small S2 signals and single electron events were falsely recognized as S1 signal by the raw data processor, the extraction anode was also flooded by an indecently risen LXe level. Which means that no extraction of the S2 signal inducing electron cloud into GXe phase can take place and so its proportional scintillate interaction is prevented.

The data sets used were acquired at different supply voltages for the PMTs which vary from 700 V to 875 V in 25 V steps. For each supply voltage one hundred data files, each containing the waveforms of 10'000 triggered events, were acquired and saved for further analysis.

After running through the raw data processor a TTree data collection structure of the ROOT toolkit for every single data file is created. These single TTrees are chained in a TChain programming structure, giving a total event count of one million triggered events per measured supply voltages for all 14 PMTs simultaneously in that TChain data structure.

4 Analysis

As mentioned in 3.3 possible SPE candidates have been observed in the Münster TPC if a signal inducing source was used at Münster's TPC [Bro13]. In this chapter the procedure of an in situ gain calibration of the PMTs of Münster's TPC is described with this SPE candidate waveforms acquired by measurements.

4.1 Single Photoelectron Events Candidates

In the sampled time interval of a raw measured waveform, multiple S1 signals can appear. Each signal is numbered, sorted from largest to smallest and filed separately into a branch of a TTree structure, so that it can be referenced later separately by its corresponding $NbS1Peaks[i]$ variable and an index i . Figure 4.1 shows an example of a processed waveform with multiple S1 like signals in it.

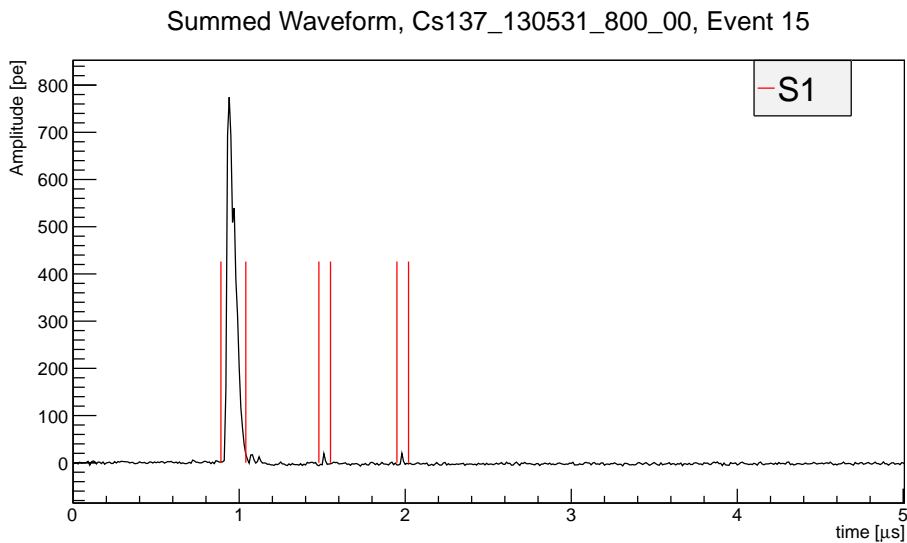


Figure 4.1:

Example of multiple S1 like events in the summed up waveform over all 14 PMTs. The second and third peak from the left are possible SPE candidates visible after placing an external calibration source in front of the detector.

To determine the gain of a given PMT, the total charge distribution of that PMT's waveform with multiple S1 signals seen in the sampled time interval is plotted. Hereby the first S1 like signal in each waveform is excluded, so that just possible SPE are

investigated. The resulting charge distribution seems to be suitable to determine the gain of the Münster's TPC PMTs, if one is expecting spectra similar to the spectra measured at room temperature with the black box method.

An example of these measured charge distributions is given in figure 4.2 which shows similarities to the “black box spectrum” in figure 4.3.

Visible on figure 4.2 is a possible SPE response at around $7.5 \times 10^6 N_e$. Also a kink appearing between the noise peak and the left half of the possible Gaussian single electron component peak is visible. Reasons for that kink are not yet known, but a promising gain analysis technique which excludes that kink, is discussed in section 4.2 of this thesis.

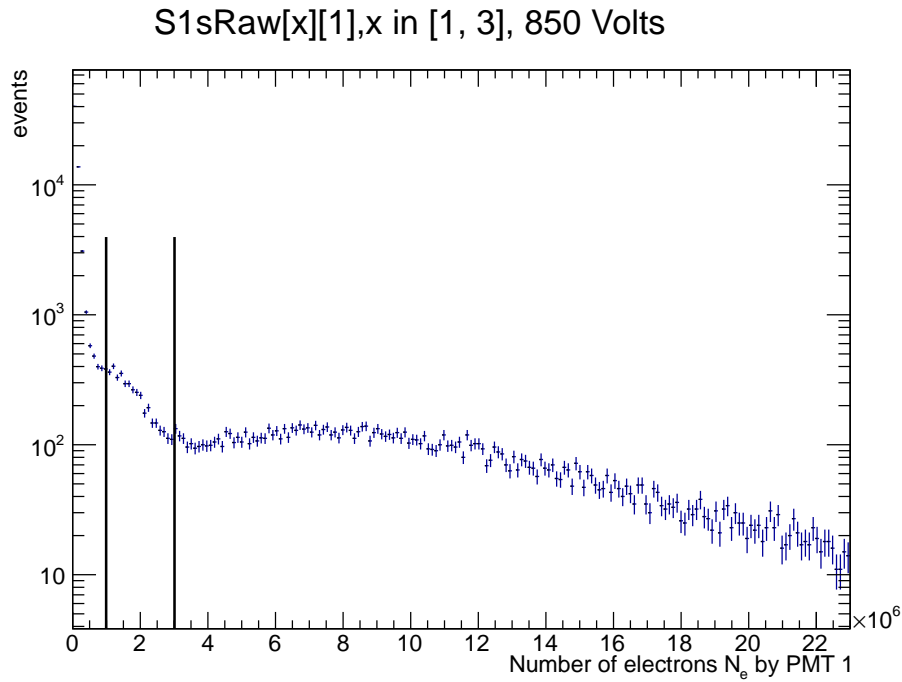


Figure 4.2:

Sample charge distribution of PMT 1 of the Münster TPC. Visible is a possible SPE peak component at around $7.5 \times 10^6 N_e$. Also a kink appearing between the noise peak and the left of the SPE component is marked by the two vertical.

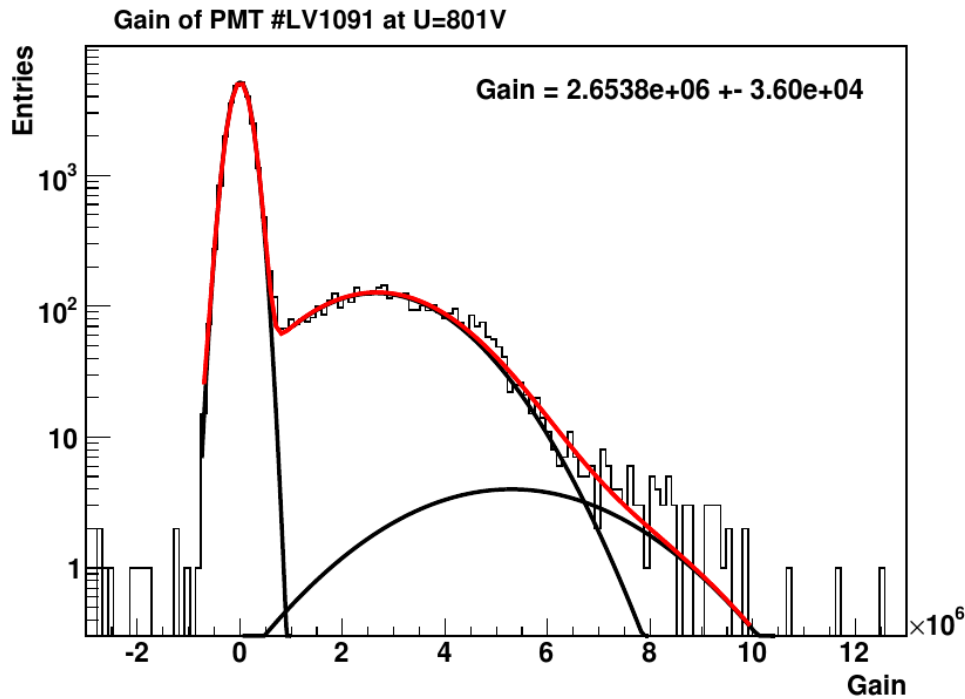


Figure 4.3:

Sample gain calibration of a PMT of the Münster TPC done by Johannes Schulz for his diploma thesis at room temperature with the dark box method. Shown is the agreement of his taken histogram data and the fit done with equation (4.1) with a noise peak, a single electron and a double electron component. Furthermore the kink linking the noise peak and the SPE component is not present in this spectrum [Sch11].

4.2 Gain Analysis of a PMT

A common way to determine the gain of a PMT is to describe its *single electron response* (SER) function as the sum of three Gaussian functions. One Gaussian for the noise peak, one Gaussian distributed peak for the single photoelectron component and one for the double photoelectron component. This function can be written as

$$g(x) = a_n \cdot \exp\left(-\frac{(x - x_n)^2}{2\sigma_n^2}\right) + a_1 \cdot \exp\left(-\frac{(x - x_1)^2}{2\sigma_1^2}\right) + a_2 \cdot \exp\left(-\frac{(x - x_2)^2}{2\sigma_2^2}\right), \quad (4.1)$$

where a_i is the amplitude of the noise peak respectively the single and double photoelectron peak, σ_i is the corresponding full width at half maximum of the peaks and x_i is representing their mean values. This ansatz contains nine free parameters to

be fitted thus a good chance is given to over minimize the resulting χ^2 value of the gain function $g(x)$. Constrains given by physically reasons can minimize this chance.

The first constrain is given by the linearity of the PMT's response function which means that x_2 can be represented by

$$x_2 = 2 \cdot x_1 . \quad (4.2)$$

Also the FWHM σ_i of the two Gaussian photoelectron response peaks are linked by Gaussian statistics as

$$\sigma_2 = \sqrt{2 \cdot \sigma_1^2} . \quad (4.3)$$

With these two constrains the resulting formula for the gain $g(x)$ can be written as

$$g(x) = a_n \cdot \exp\left(-\frac{(x - x_n)^2}{2\sigma_n^2}\right) + a_1 \cdot \exp\left(-\frac{(x - x_1)^2}{2\sigma_1^2}\right) + a_2 \cdot \exp\left(-\frac{(x - 2x_1)^2}{4\sigma_1^2}\right) , \quad (4.4)$$

with just seven free parameters being left.

The gain and its error of a PMT is then given by the fit parameter x_1 representing the mean of the Gaussian distributed single electron component.

Using equation (4.4) J. Schulz has determined the gains of the Münster TPC's PMTs in his diploma thesis [Sch11] in a dark box at room temperature as described in chapter 2.4.2. An example of his gain determination, by using this seven free parameter SER function is given in figure 4.3.

This gain equation though showing good results in an external dark box, does not nicely represent the measured energy spectra using the secondary S1 events appearing inside the Münster TPC's detector. This results mainly because of the extra kink given by an unknown event population in an charge range between the noise and the SPE component as shown in figure 4.2.

A way to do a proper in situ gain determination with the given data is to adapt the equation (4.4) by removing its noise peak component which yields to the equation

$$g(x) = a_1 \cdot \exp\left(-\frac{(x - x_1)^2}{2\sigma_1^2}\right) + a_2 \cdot \exp\left(-\frac{(x - 2x_1)^2}{4\sigma_1^2}\right) . \quad (4.5)$$

Since that equation is no longer describing the whole spectrum, because it is not taking the noise peak and the unknown event population, i. e. the kink in the spectra, into account, the statistical error of the fit done by equation (4.5) against the measured spectra is by its own no longer a reliable error estimation of the true gain value. To give an appropriate error estimation, the impact of the kink and the noise peak on the gain has to be estimated probably.

The systematic errors are hence analysed by varying the fit range starting point of equation (4.5) on the given spectra. Thus one can give an estimation of the influence

of the noise peak and the extra population represented by the kink in the spectra for the gain of a PMT and its fit done with equation (4.5).

As a proper variation range of the fit starting point, the range of bins between a bit right to the best valley estimation and a bit left to the best hill position of the SPE component were chosen by looking at each of the individual measured energy spectra.

In figure 4.4 two examples of a PMT of the Münster TPC are given, using this method of error estimation. The vertical lines in both figures represent the range of variation of the fit range starting point. Whereas the black peaks represent the SPE (dotted) and the double photoelectron event (dashed) components for the lowest value of the starting point inside the fit range and the grey peaks represent the according SPE and double photoelectron component for a fit with the maximum value of the starting point inside the fitting range. The black and the grey lines represent equation (4.5), i. e. the sum of both appropriate components, for the fit start point being the minimum in the fitting range, respectively being its maximum value.

Having both subfigures side by side one can clearly see that the kink of the unknown extra population is becoming more dominant for higher voltages and the influence of the kink on the error of the gain is hence increasing with higher voltages, too.

The gain's g total error Δg can therefore be described by its statistical error σ_{stat} and systematic error σ_{sys} like

$$g \pm \Delta g = g \pm \sigma_{stat} \pm \sigma_{sys} . \quad (4.6)$$

The gain g is the mean of all single gains g_i from the variation of the start point of the fitting range expressed by the formula

$$g = \frac{1}{n} \sum_{i=0}^n g_i , \quad (4.7)$$

with i running over all n fits done by varying the fit starting point.

The statistical error σ_{stat} of the gain g is the Gaussian error propagation of every single fit error of the calculated gains as given by

$$\sigma_{stat} = \sqrt{\frac{1}{n^2} \sum_{i=0}^n (\Delta g_i)^2} , \quad (4.8)$$

with Δg_i being the fit error of the gain g_i representing one of the fits in the varying range of the fit starting points.

The systematic error σ_{sys} of this method is given by the standard deviation of the mean gain g given by the formula

$$\sigma_{sys} = \sqrt{\frac{1}{1-n} \sum_{i=0}^n (g_i - g)^2} . \quad (4.9)$$

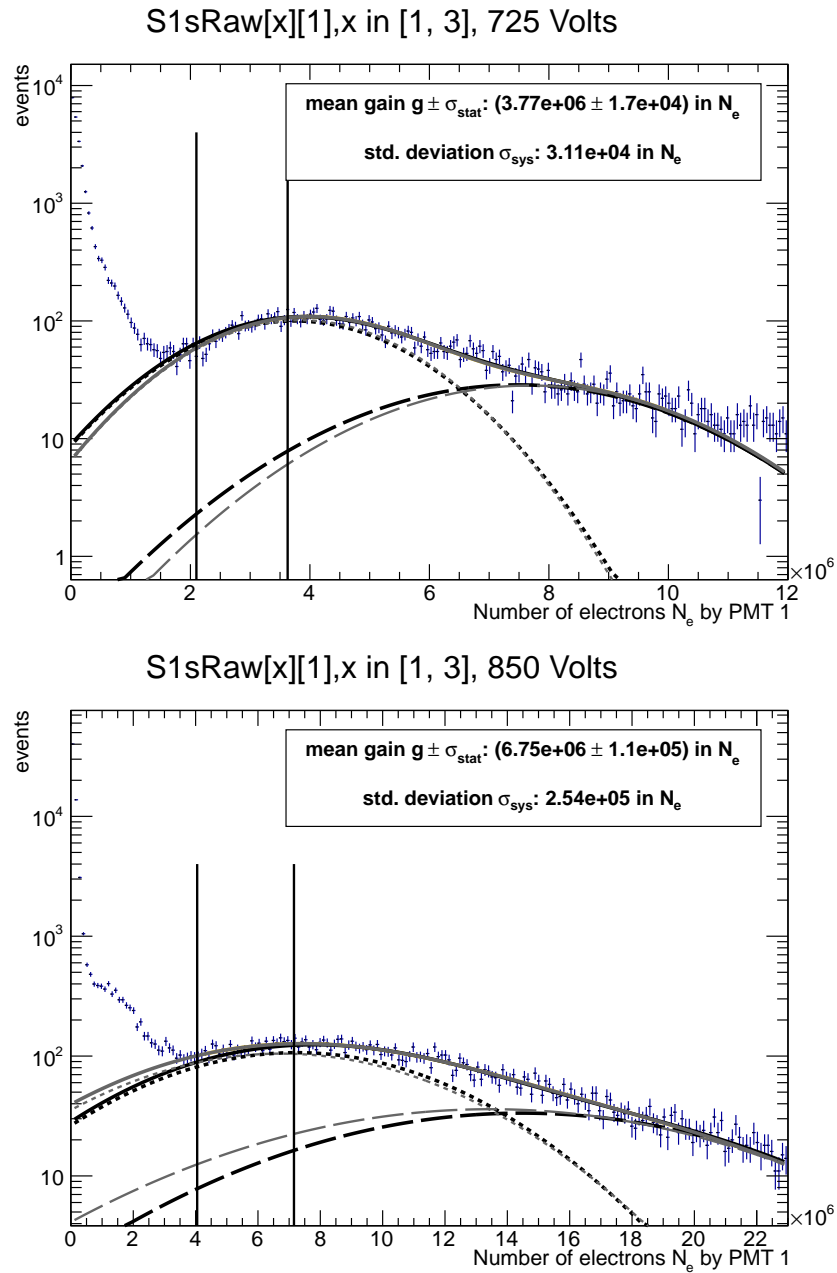


Figure 4.4:

Two example spectra of the charge distribution of PMT 1 of the Münster TPC. One with a supply voltage of 725 V and one with 850 V. The vertical lines represent the range of variation of the fit range starting point. The black peaks represent the SPE (dotted) and the double photoelectrons (dashed) components for the lowest value of the starting point, the grey peaks represent the according SPE and double photoelectron component for a fit with the maximum value of the starting point inside the fitting range. The black and the grey lines are the sum of the both appropriate components.

4.3 Gain Equilibration of a PMT

Knowing the gains for different supply voltages applied to a PMT one could simply use that knowledge for further experiments with these PMTs.

Nevertheless, it is preferred for a detector like the Münster TPC, which is working with fourteen PMTs, to get a charge response from each PMT within a similar dynamic range. An additional constrain on that range is that it is preferable to use a supply voltage which is high enough to get a good charge output per incident photon from each PMT without the voltage being too high, so that one is getting non linear effects into the PMT's response function. For the Münster TPC a gain g of $2 \times 10^6 N_e$ is favoured [Sch11].

As mentioned in section 2.4.2 by equation (2.12) the gain g of a PMT by a given supply voltage U of the PMT can be expressed by a power law of the form

$$g = A \cdot U^k, \quad (4.10)$$

with A being an amplification factor and k being a parameter determined by the material, structure and number of the dynodes.

Thus knowing the gains g for certain voltages U the parameters of the power law of equation (4.10) can be extrapolated by fitting the data with this equation. An example of one of these fits done with respect to the measured data is shown in figure 4.5.

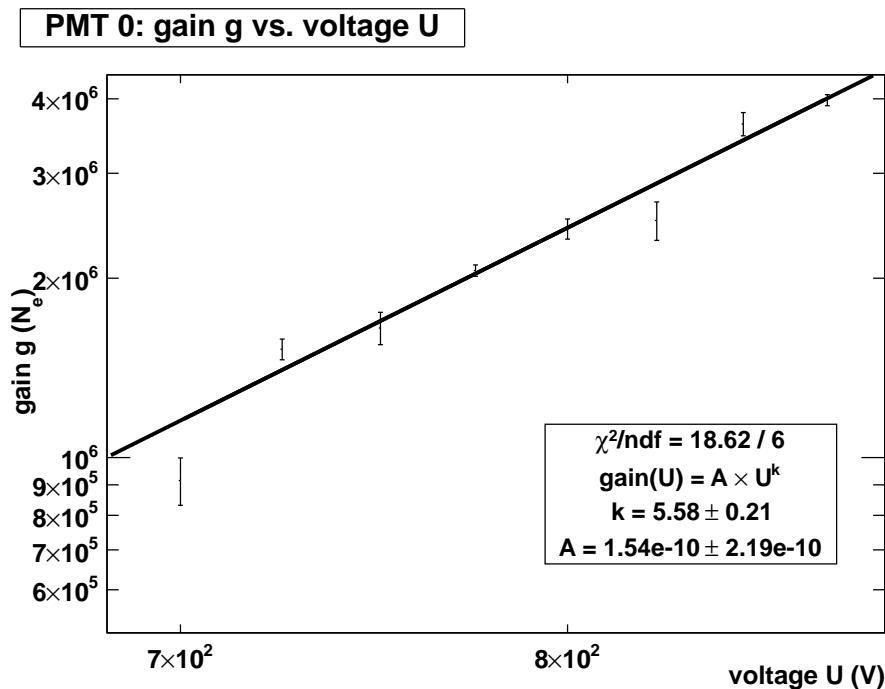


Figure 4.5:

Example of the gain versus supply voltage fit done with equation (2.12) for PMT 0 of the Münster TPC. Using the fit result one can set the gain of PMT 0 to the desired value of $2.0 \times 10^6 N_e$.

4.4 Event Distributions Analysis

If one is assuming a Gaussian shaped noise peak and a Gaussian shaped SPE and double electron event peak, like it is done in parts of the gain analysis described in section 4.2, the mentioned kink from example figure 4.2 is worsening the peak to valley ratio of the single electron component peak. If one would know exactly which events, that happen inside the Münster TPC, are causing this extra population in the spectra, one could cut out this unwanted event distribution and then redo the gain determination with equation (4.1) containing the noise peak and most likely get a narrow error margin on the gain. Alternatively one could maybe get at least a better peak to valley ratio for the SPE peak thus getting a better estimation with the non-noise peak fit described by equation (4.5).

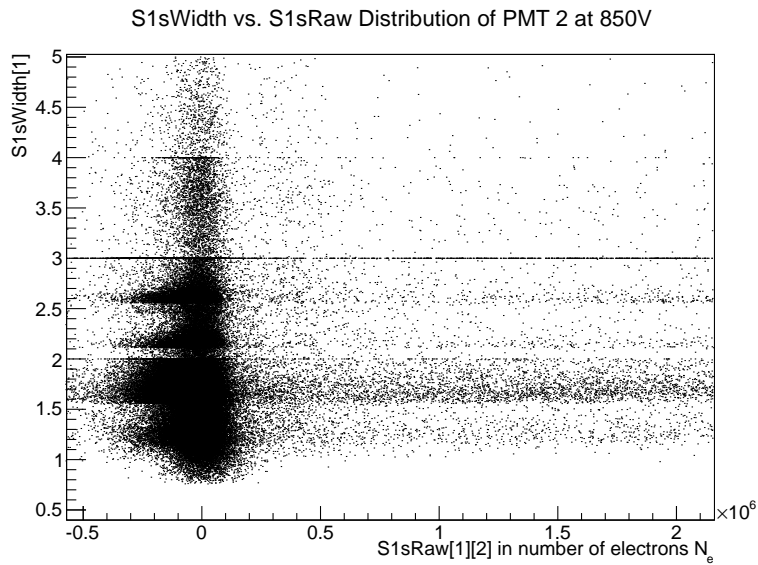
For the further analysis of the PMTs of Münster's TPC, reasons for the extra kink population has been investigated by looking at different parameter distributions of the acquired data. Namely this were the distributions of the signal's width of the first S1 signal versus the raw ADC counts of the secondary S1 signal inside one sampled waveform and the distribution of distance in time between the ending of the first and the beginning of the second S1 signal sampled in one waveform versus the raw ADC counts of the secondary S1 signal.

Both distributions are showing artefacts in the form of events showing up or being missing preferred on certain horizontal lines throughout the whole spectrum. This is shown in figure 4.6 exemplary for PMT 2 of the Münster TPC.

Cutting out the events being added, by the lines visible in the S1 width distribution of figure 4.6a, show no remarkable positive or negative impact on the energy spectra that are used for the following gain calibration. This is reasonable since the cut out events are uniformly distributed over the whole spectrum.

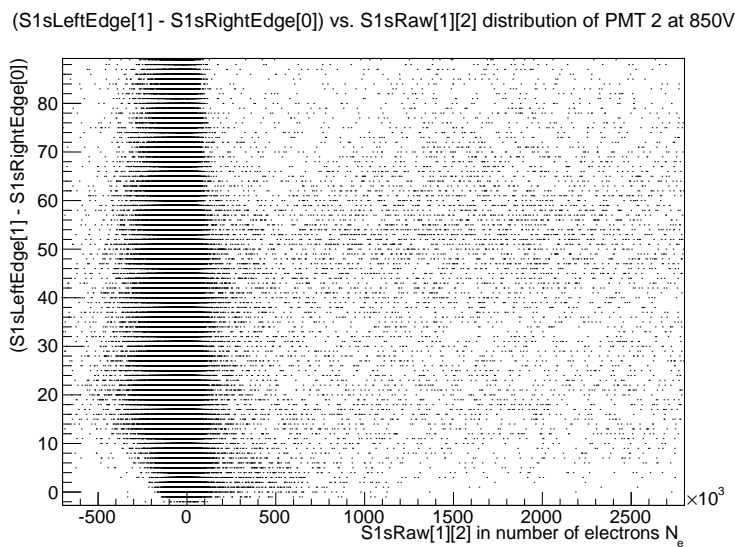
Further investigations of the numerical values of these events on each one of this lines showed that their value is exactly the same for all significant digits. This issue has been investigated by Ethan Brown, who traced it back to calculations with quantized variables, so that quantized structures are expectable [Bro13].

Further cuts on single possible event distributions, which means on cluster like accumulations of points seen in the plotted event distributions of these spectra, has been probed in order to get a clue about the reasons for the kink. But all cuts done showed no positive effect on the spectra quality concerning the removal of the extra population showing up as a kink inside them. Thus, the following analysis were performed without applying such data selection cuts.



(a)

Distributions of the signal's width of the first S1 signal versus the raw ADC counts of the secondary S1 signal inside one sampled waveform. Visible are the raw data processors quantized calculations showing up in the form of black lines inside the spectrum.



(b)

Distribution of the distance in time between the ending of the first and the beginning of the second S1 signal sampled in one waveform versus the raw ADC counts of the secondary S1 signal. Visible is the quantized structure of the spectrum.

Figure 4.6:

Two different example event distributions of PMT 2 of the Münster TPC from the data sets measured with a PMT supply voltage of 850 V.

4.5 Results of the Bottom PMTs

The results of the used method to determine the gains of the bottom PMTs in Münster's TPC in situ yield to gains in a range of approximately $1.0 \times 10^6 N_e$ to $5.0 \times 10^6 N_e$ in a voltage range of 700 V to 875 V in most of the cases. That seems reasonable compared to the gains determined by Johannes Schulz in his diploma thesis [Sch11].

By fitting these gains for each of the seven bottom PMTs of Münster's TPC with the power law of equation (4.10), one can determine the supply voltage U of the given PMT that fits the desired gain of $2.0 \times 10^6 N_e$ the most.

An example of that gain g versus voltage U fit is given in figure 4.5 for PMT 0 of the Münster TPC.

The supply voltages of the bottom PMTs of Münster's TPC are then calculated from the fits done using equation (4.10) to give a charge response of $2.0 \times 10^6 N_e$ wherever possible. Two PMTs, namely PMT 2 and PMT 3, could not be set to a charge response of $2.0 \times 10^6 N_e$ for a SPE because their dynamic range was either too high or too low. Their voltage U was chosen so that their response function is as close to $2.0 \times 10^6 N_e$ in charge output for a SPE as possible. An overview of all seven bottom PMTs and their set voltages at the power supply for an equilibrated common gain of approximately $2.0 \times 10^6 N_e$ is given in table 4.1.

Table 4.1:

Overview of the supply voltages for the Münster TPC's bottom PMTs that were set to yield to an equalized gain of $2.0 \times 10^6 N_e$. For the two PMTs which gain cannot be set to $2.0 \times 10^6 N_e$, the gain that is closest to it is chosen.

No. PMT	Supply Voltage U of the PMT in Volt	approx. Gain g in N_e
PMT 0	772 V	2.0×10^6
PMT 1	700 V	3.2×10^6
PMT 2	900 V	1.7×10^6
PMT 3	768 V	2.0×10^6
PMT 4	707 V	2.0×10^6
PMT 5	788 V	2.0×10^6
PMT 6	731 V	2.0×10^6

4.6 Results of the Top PMTs

While the determination of gains for different PMT supply voltages of the bottom PMTs of Münster's TPC with equation (4.10) and its described error estimation worked well, it does not show plausible results for the top PMTs of Münster's TPC. This is because the spectra for the top PMTs differ in several points from the spectra of the bottom PMTs.

To mention is that there are spectra in which there is no valley between the noise peak and the single photoelectron component of the SER function for any given voltage of a PMT (see example given in figure 4.7).

Another observation in some of the spectra is, that the extra kink in the spectra becomes a Gaussian like peak for higher PMT supply voltages. This is shown exemplary in figure 4.8.

Nevertheless, fits were performed wherever possible. If the fits could not converge with the method used for the bottom PMTs, subjective chosen constrains were used. That means, a bin range was searched in which a subjective appropriate convergence was given.

Two problems were common while doing the fits of the top PMTs. The first one is, that even with the applied constrains, no convergence of the fit was reach for many spectra that suits the given data distribution. The second one is, that the found single photoelectron component of the SER function converges into the Gaussian peak, which most likely is the former kink like anomaly.

Due to the importance of knowing the gains of the PMTs for the further use of the detector, the gains of the top PMTs are estimated at least to an order of magnitude by the given data. Either by using the fits that converged or by choosing visually the subjective most likely mean gain value from the spectra in which the fits did not converge.

These *estimated* gains for the top PMTs are listed in table 4.2. Since this gain values are based upon very subjective decisions, non objective error estimation can be given.

Table 4.2:

The following table is showing the subjectively judged order of magnitude for the gains of the top PMTs by their spectra. It is no error given, because no adequate way to determine the error can be named.

No. PMT	Supply Voltage U of the PMT in Volt	approx. Gain g in N_e
PMT 7	900 V	2×10^5
PMT 8	900 V	2×10^5
PMT 9	900 V	2×10^5
PMT 10	dead	dead
PMT 11	900 V	2×10^5
PMT 12	800 V	2×10^6
PMT 13	775 V	2×10^6

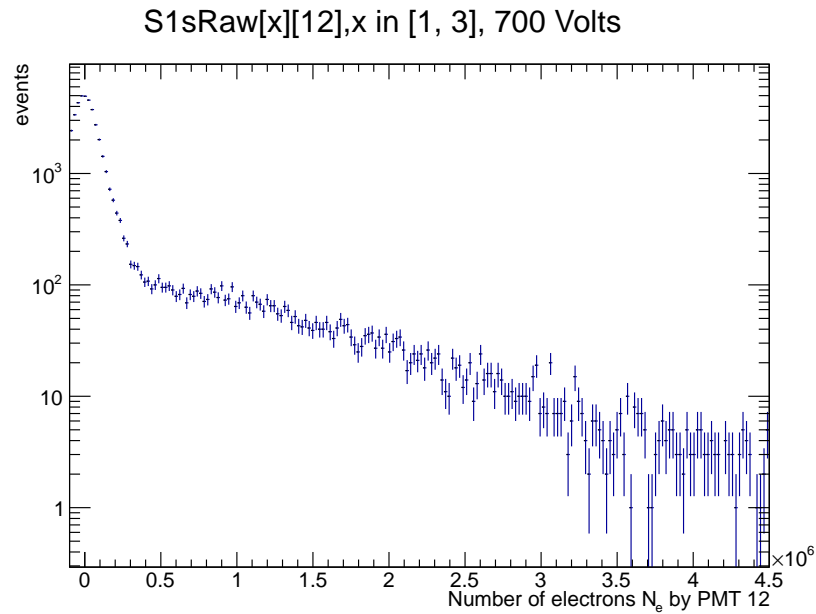


Figure 4.7:

Example charge distribution of PMT 12 with a supply voltage of 700 V showing a needles junction between the noise and the possible SPE component, without any valley or longer plateau between them.

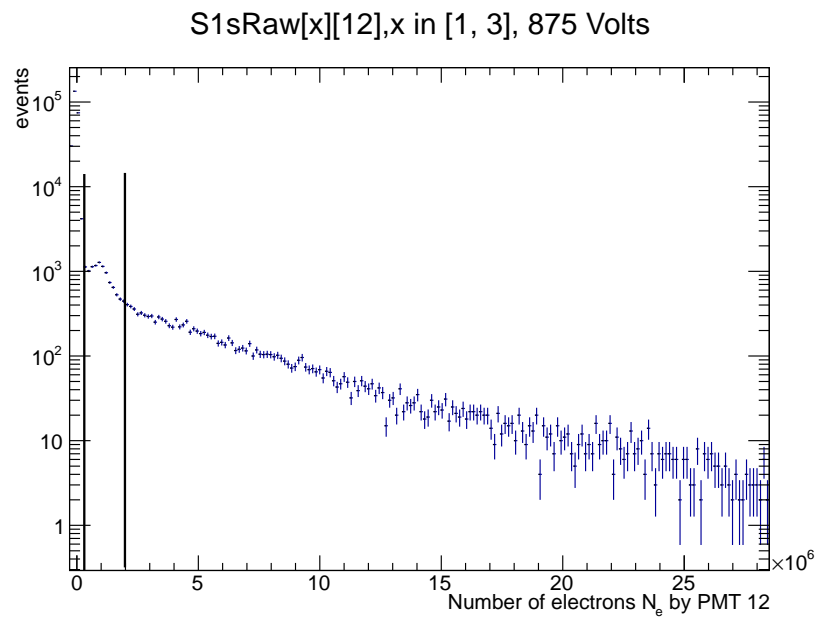


Figure 4.8:

Example charge distribution of PMT 12 with a supply voltage of 875 V showing the kink inducing population forming a Gaussian like peak component in the spectrum, marked by the vertical lines.

5 Summary and Outlook

Within this bachelor thesis the possibility of an in situ characterization of the PMTs of the Münster TPC is investigated and it is shown that this technique yields to a proper gain calibration for the bottom PMTs, but not for the top PMTs of the Münster TPC.

It is shown that inside the detector secondary S1, SPE like, events appear while a Cs137 source is placed outside the detector. Furthermore a way to measure the SER function for this secondary SPE is explained and a technique to do a gain calibration and equilibration with that SER function is presented.

The analysis of the charge spectra for the selected secondary S1 signals show suitable distributions for applying a SER function made of two Gaussian peaks, one representing its single photoelectron component and one representing its double photoelectron component. Because of an unknown signal population appearing as a kink in the charge range between the noise and the single photoelectron component peak, a third Gaussian function representing the noise component is not used, which led to equation (4.5).

For a proper error estimation of the determined gains from equation (4.5), its fit range starting point is varied in a range between the minimum event count rate between the kink and the single photoelectron component peak and the mean value of the single photoelectron component peak. The mean of the determined gains for a given spectrum are thus representing the most possible gain values and the Gaussian error propagation of the single fit errors are representing their statistical error. Additionally, the standard deviation of the determined mean gain is used as a value to describe its systematic error.

For the bottom PMTs of the Münster TPC this yields a maximum error of 15 % in rare cases and a total error below the 5 % mark in most cases for the gains of a PMT at a given supply voltage.

With the determined gains for different supply voltages of the bottom PMTs of the Münster TPC a gain equilibration is done and the supply voltage to set for each bottom PMT for a gain of $2.0 \times 10^6 N_e$ is determined. At this point it becomes apparent that PMT 1 with a minimum gain of $3.2 \times 10^6 N_e$ at a voltage of 700 V and PMT 2 with a maximum gain of $1.7 \times 10^6 N_e$ at a voltage of 900 V cannot be set to the desired gain of $2.0 \times 10^6 N_e$.

The analysis of the top PMTs with this technique does not work. Problems that show up are the in general low gains of the top PMTs over all supply voltages and the relative more dominant influences of the kink inside the spectra compared to the bottom PMTs. Furthermore no trustworthy range of convergence for the fits done with equation (4.5) are found in most cases.

Thus only a subjective and no more than most likely order of magnitude for the

gains of the top PMTs can be stated within this thesis.

Based on the results of this thesis, some questions about the behaviour of the Münster TPC cannot be answered and new question arises.

Since the bottom PMTs gain can be determined upon a solid basis as shown in this thesis, the next goal should be to find a way to determine the gain of the top PMTs appropriately.

A possible next step to do so, is to investigate the source of the extra population, that appears as a kink in the measured charge spectra of the PMTs.

By finding a way to cut out these events or by knowing more of the influence of them concerning the SER function of a PMT, the systematic errors on the PMTs' gains can likely be decreased. In consequence a gain equalization for the top PMTs could be more promising.

An additional investigation for the reasons of the low gain responses of most top PMTs and thus their overall less convincing spectra can be another key to determine their gains.

One possible way to get a hand on what is happening with the top PMTs, can be to rise the LXe level inside the detector until the top PMTs are surrounded by the LXe phase and try to find out, if and why the SRE function of the top PMTs then changes.

Additionally other techniques for a in situ calibration or ways to refine the in situ calibration technique of this thesis must be thought off to minimize the overall error on the determined gains.

After solving the mentioned problems and having a proper gain calibration for the top PMTs, the Münster TPC can efficiently be used for research and development tasks for the XENON1T experiment due to Münster's participation of the XENON Collaboration.

Tasks like electron lifetime measurements that give information about the purity of the xenon recirculation through the detector or light yield measurements for spectroscopy reasons and thus looking for radioactive isotopes inside the detector, are just two of a lot of more possible uses of the Münster TPC.

A Photo of the Münster TPC

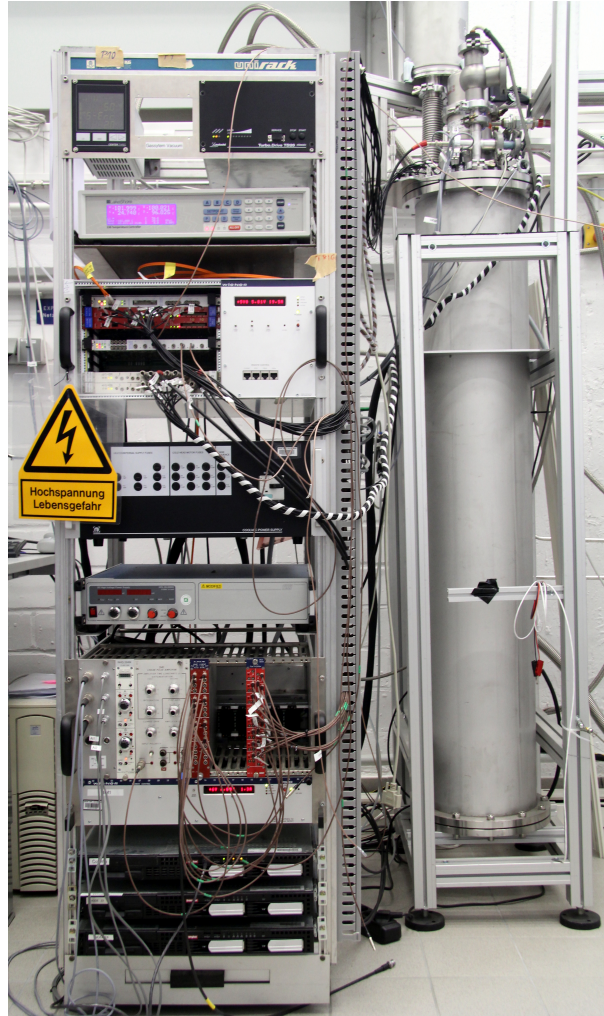


Figure A.1:

Photo of the Münster TPC standing in the Münster XENON laboratory. The vacuum insulation vessel with the Münster TPC inside is shown on the right. On the left the data acquisition unit and the high voltage supply are located inside the rack. The photo's ownership belongs to the Münster XENON group (2013, file location: *nustorage://inbox/XENON/muenster_lab_051013*).

Bibliography

- [A⁺10] E. Aprile et al. Technical Design Report of XENON1T at LNGS. Technical report, LNGS, October 2010.
- [A⁺11] E. Aprile et al. Design and Performance of the XENON10 Dark Matter Experiment. *Astropart. Phys.*, 34:679–698, 2011.
- [AD09] E. Aprile and T. Doke. Liquid Xenon Detectors for Particle Physics and Astrophysics. *Rev.Mod.Phys.*82:2053-2097,2010, 2009.
- [B⁺91] K. G. Begemann et al. Extended Rotation Curves of Spiral Galaxies - Dark Halos and Modified Dynamics. *Mon. Not. R. Astron. Soc.*, 249:523–537, 1991.
- [Bro13] Brown, Dr. Ethan; University of Münster, Institut für Kernphysik. Personal communication, 2013.
- [C⁺06] Douglas Clowe et al. A Direct Empirical Proof of the Existence of Dark Matter. *Astrophys.J.*648:L109-L113, 2006.
- [DAPR11] R. M. Dunstan, K. N. Abazajian, E. Polisensky, and M. Ricotti. The Halo Model of Large Scale Structure for Warm Dark Matter. *ArXiv e-prints 1109.6291v1*, September 2011.
- [Ein36] Albert Einstein. Lens-Like Action of a Star by the Deviation of Light in the Gravitational Field. *Science*, 84:506, 1936.
- [ESA13] ESA and Planck Collaboration. ESA Science & Technology: Planck. online, 2013. <http://sci.esa.int/planck/>, visited 23.09.2013.
- [Gam48] G. Gamow. The Origin of Elements and the Separation of Galaxies. *Phs. Rev.*, 75:505, 1948.
- [Ham07] Hamamatsu Photonics K. K. *Photomultiplier Tubes; Basics and Applications*, 3 edition, 2007.
- [JKG96] G. Jungman, M. Kamionkowski, and K. Griest. Supersymmetric Dark Matter. *Physics Reports*, 267:195–373, March 1996.
- [Kit10] Charles Kittel. *Introduction to Solid State Physics*. Wiley John + Sons, 8th edition, 2010.

-
- [L⁺13] LUX Collaboration et al. First results from the LUX dark matter experiment at the Sanford Underground Research Facility. *ArXiv e-prints 1310.8214*, October 2013.
- [Mas08] Andrew Massari. PMT Gain Calibration for XENON100. *University of Notre Dame*, August 2008.
- [Oor32] Jan Oort. Note on the Difference in Velocity between Absolutely Bright and Faint Stars. New Haven, Yale University Observatory, 1932.
- [OS03] J. P. Ostriker and P. Steinhardt. New Light on Dark Matter. *Science*, 300:1909–1914, June 2003.
- [PA⁺13] Planck Collaboration, P. A. R. Ade, et al. Planck 2013 results. XVI. Cosmological parameters. *ArXiv e-prints 1303.5076*, March 2013.
- [Pla12] Guillaume Plante. *The XENON100 Dark Matter Experiment: Design, Construction, Calibration and 2010 Search Results with Improved Measurement of the Scintillation Response of Liquid Xenon to Low-Energy Nuclear Recoils*. PhD thesis, Columbia University, 2012.
- [PW65] A. A. Penzias and R. W. Wilson. A Measurement of Excess Antenna Temperature at 4080 Mc/s. *Astrophys. J.*, 142:419, 1965.
- [RF70] Vera C. Rubin and W. Kent Jr. Ford. Rotation of the Andromeda Nebula from a Spectroscopic Survey of Emission Regions. *Astrophysical Journal*, 159:379, February 1970.
- [S⁺04] V. N. Solovov et al. Measurement of the Refractive Index and Attenuation Length of Liquid Xenon for its Scintillation Light. *Nucl. Instr. Meth. Phys. Res. Sect. A*, 516:462, 2004.
- [Sch11] Johannes Schulz. *Design of a 2-Phase Xenon Time Projection Chamber for Electron Drift Length Measurements*. Institut für Kernphysik, Westfälische Wilhelms-Universität Münster, December 2011.
- [WFD83] S. D. M. White, C. S. Frenk, and M. Davis. Clustering in a Neutrino-Dominated Universe. *Astrophysical Journal, Part 2 - Letters to the Editor*, 274:L1–L5, November 1983.
- [XA⁺12a] XENON100 Collaboration, E. Aprile, et al. Dark Matter Results from 225 Live Days of XENON100 Data. *Physical Review Letters*, 109(18):181301, November 2012.
- [XA⁺12b] XENON100 Collaboration, E. Aprile, et al. The XENON100 Dark Matter Experiment. *Astroparticle Physics*, 35:573–590, April 2012.
- [Zwi37] F. Zwicky. On the Masses of Nebulae and of Clusters of Nebulae. *Astrophysics Journal*, 86:217, October 1937.